UNIVERSITY OF CALIFORNIA

Los Angeles

The Physics of Beat Excited Plasmas

A dissertation submitted in partial satisfaction of the

requirements for the degree
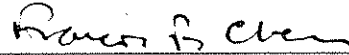
Doctor of Philosophy in Electrical Engineering

by

Matthew James Everett

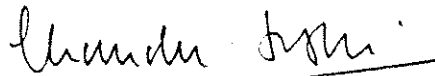1994

The dissertation of Matthew James Everett is approved.

Francis F. Chen

Francis F. Chen

John M. Dawson

John M. Dawson

Chan Joshi

Chan Joshi, Committee Chair

University of California, Los Angeles

1994

ii

DEDICATION

To my parents, Pat and Meryl.

For Tonja.

Contents

List of Figures

ACKNOWLEDGMENTS

I would first like to express my gratitude towards my advisor Professor Chan Joshi both for his help and guidance throughout my career as a graduate student at UCLA and for providing such a supportive and well equipped laboratory environment without which this thesis would not have been possible. Many thanks to Chris Clayton and Ken Marsh for all of their help in the lab and for teaching me most of what I know about doing experiments. Also thanks to Amit Lal for always being willing to lend a hand and for his detailed editing and correcting of publications. I appreciate the support running PIC simulations from Warren Mori and the discussions of theory with him which helped me develop a better understanding of plasma physics. To Professor Francis Chen, thank you for the excellent classes which developed my interest in this field. I am also thankful to Maria Guerrero for her administrative support.

Finally thanks to my wife, Tonja, for all of her patience and support while I was struggling through writing my thesis.

VITA

June 20, 1965   Born, Waltham, Massachusetts

1987   B.S., Electrical Engineering

University of Michigan Ann Arbor

1987-1988   Micro Fellowship

1988-1991   National Science Foundation Fellowship

1992   M.S., Electrical Engineering

University of California Los Angeles

1991-1994   Graduate Research Assistant

Department of Electrical Engineering

University of California, Los Angeles

PUBLICATIONS

C. E. Clayton, K. A. Marsh, A. Dyson, M. J. Everett, A. Lal, W. P. Leemans, R. Williams, T. Katsouleas, and C. Joshi, "Recent results on the beat wave acceleration of externally injected electrons in a plasma.", 1992 Linear Accelerator Conference Proceedings (AECL-10728)

C. E. Clayton, K. A. Marsh, A. Dyson, M. J. Everett, A. Lal, W. P. Leemans, R. Williams, and C. Joshi, "Ultrahigh-gradient acceleration of injected electrons by laser-excited relativistic electron plasma waves.", Physical Review Letters, 4 Jan. 1993, vol.70, (no.1):37-40.

C. Joshi, C. E. Clayton, K. A. Marsh, A. Dyson, M. J. Everett, A. Lal, W. P. Leemans, R. Williams, T. Katsouleas, and W. B. Mori, "Acceleration of injected electrons by the plasma beat wave accelerator.", (Third Advanced Accelerator Concepts Workshop, Port Jefferson, NY, USA, 14-20 June 1992). AIP Conference Proceedings, 1993 (no.279):379-410.

C. E. Clayton, K. A. Marsh, A. Dyson, M. J. Everett, A. Lal, W. P. Leemans, R. Williams, and C. Joshi, "Experimental demonstration of laser acceleration of electrons via relativistic plasma waves.", (Short-Pulse High-Intensity Lasers and Applications II, Los Angeles, CA, USA, 21-22 Jan. 1993). Proceedings of the SPIE - The International Society for Optical Engineering, 1993, vol.1860:32-45.

S. C. Hartman, N. Barov, C. Pellegrini, S. Park, J. Rosenzweig, G. Travish, R. Zhang, C. E. Clayton, P. Davis, M. J. Everett, C. Joshi, and G. Hairapetian, "Initial measurements of the UCLA RF photoinjector.", (High Intensity Electron Sources, Legnaro, Italy, 24-28 May 1993). Nuclear Instruments & Methods in Physics Research, Section A (Accelerators, Spectrometers, Detectors and Associated Equipment), 11 Feb. 1994, vol.340, (no.1):219-30.

M. J. Everett, A. Lal, D. Gordon, C. E. Clayton, K. A. Marsh, and C. Joshi, "Trapped electron acceleration by a laser-driven relativistic plasma wave.", Nature, 7 April 1994, vol.368, (no.6471):527-9.

C. E. Clayton, M. J. Everett, A. Lal, D. Gordon, K. A. Marsh, and C. Joshi, "Acceleration and scattering of injected electrons in plasma beat wave accelerator experiments.", (35th Annual Meeting of the Division of Plasma Physics of the American Physical Society, St. Louis, MO, USA, 1-5 Nov. 1993).

M. J. Everett, A. Lal, C. E. Clayton, W. B. Mori, C. Joshi, and T. Johnston, "Dynamics of the resonantly excited relativistic plasma wave driven by a CO_2 laser", Submitted to Physics of Plasmas

M. J. Everett, A. Lal, D. Gordon, K. Wharton, C. E. Clayton, W. B. Mori, and C. Joshi, "Evolution of stimulated Raman into stimulated Compton scattering of laser light via wave-breaking of plasma waves", Submitted to Physical Review Letters

M. J. Everett, A. Lal, C. E. Clayton, W. B. Mori, and C. Joshi, "Coupling between high-frequency plasma waves in laser-plasma interactions", Submitted to Physical Review Letters

ABSTRACT OF THE DISSERTATION

The Physics of Beat Excited Plasmas

by

Matthew James Everett

Doctor of Philosophy in Electrical Engineering

University of California, Los Angeles, 1994

Professor Chan Joshi, Chair

Physics issues associated with plasma beat-wave acceleration of electrons are studied through experiments, theory, and simulations. In the experiments, a beat-wave is driven in a plasma formed by tunneling ionization with an intense short pulse two frequency CO_2 laser (100 Joules in 350 psec (FWHM)). The time evolution of this wave including its amplitude of $33\pm11\%$ and duration of 100 psec (FWHM) is measured via direct Thomson scattering of a 0.532 μm probe laser. Particle-in-cell (PIC) code simulations with realistic time scales are used to study the dynamics of the wave and pinpoint expulsion of the plasma by the ponderomotive force of the laser and beat-wave as the limiting factor in amplitude and duration of the wave. This wave is used to trap and accelerate an externally injected relativistic electron beam for the first time, producing energy gains of 28 MeV over 1 cm. This is more than 100 times the acceleration gradients of $\approx$20 MeV obtained in conventional RF electron accelerators such as the Stanford Linear Accelerator/Collider.

Experimental evidence for the coupling of the relativistic phase velocity beat-wave to low phase velocity electron plasma waves associated with the Raman backscatter instability is presented using time and wavenumber resolved spectra of Thomson scattered light from the plasma. The qualitative features of the measured $w(t, k)$ spectra are predicted by a Lagrangian coordinate description and reproduced in particle simulations which show that the daughter waves generated in the mode coupling process take the energy preferentially from the Raman wave without significantly affecting the beat-wave.

The evolution of the stimulated Raman backscatter instability of laser light into Compton scattering in an initially cold plasma is also studied through experiments and simulations. The simulations show that the key to the evolution of the $w(t, k)$ spectra is wave-breaking of Raman plasmons, which accelerates some electrons up to 4 times the Raman phase velocity, and the consequent return current of the bulk plasma electrons in the opposite direction. This causes a downshift in the Raman frequency during wave-breaking seen both in the simulations and the experiments.

Chapter 1

Introduction

Since the development of the first electron accelerator by John Cockcroft and Ernest Wolton in 1932, the electron energies obtained through acceleration have grown exponentially from 1 MeV in 1932 to 50 GeV obtained by the Stanford Linear Accelerator/Collider (SLAC) in 1992. However, further growth in the energy of electrons produced by such accelerators has been stymied recently by the cost of producing ever larger and more expensive accelerators. The acceleration gradients in conventional slow wave accelerating structures is limited to about 20 MeV/m by RF breakdown on the walls of the structure. Thus a state of the art electron accelator such as SLAC requires an acceleration length of about three kilometers to obtain 50 GeV with an acceleration gradient of 17 MeV/m. For protons, this problem of acceleration gradients can be alleviated somewhat by accelerating the particles in a circle and thus repeatedly reusing the same acceleration structure to drive particles to ever increasing energies. Fermi National Accelerator Laboratory in Illinois, for instance, uses this method to accelerate protons up to 1 TeV in a circular structure 4 miles in circumference. However,

synchotron radiation losses limit the energy of these circular accelerators and make them impractical for the acceleration of light particles such as electrons.

To make continued gains in electron energy without building ever larger and more expensive accelerators, the limits to acceleration gradients imposed by RF breakdown must be overcome. One solution, proposed by T. Tajima and J. M. Dawson in 1979, is to accelerate the electrons inside a plasma which can sustain much larger fields than conventional structures[1]. In this scheme an injected electron beam is accelerated by the longitudinal electric fields associated with a relativistic plasma wave driven either by an ultra-short laser pulse or a series of such laser pulses generated by the beating of two laser pulses of slightly different frequencies. Although such plasma beat-waves had been generated in the United States[2], England[3], Japan[4], and France[5], the first proof of principle experiment involving acceleration of an injected electron beam by these beat-waves was not accomplished until 1993 by a research group under Professor Chan Joshi at UCLA.

This thesis describes the effort involved in transforming the beat-wave accelerator from a proof of principle experiment into a useful accelerator. To increase the quantitative understanding of the physics of the beat-wave accelerator, it is important to develop diagnostics which can accurately measure the amplitude and time evolution of the beat-wave. Simulations must also be developed to model the beat-wave accurately and determine what effects limit the beat-wave amplitude and duration. This information is critical for developing and evaluating the feasibility of future beat-wave accelerator designs. In Chapter 2 a direct time-resolved beat-wave amplitude diagnostic based on small angle Thomson scattering of a probe laser from the beat-wave is presented in addition to

2

measurements of the effect of the beat-wave on the injected electron beam and one to one particle-in-cell 2D (PIC) simulations of the beat-wave. The Thomson scattering provides an estimate of the beat-wave amplitude between 22% and 44% and duration of 100 psec (FWHM), while the simulations predict an amplitude of 26% and indicate that expulsion of the plasma by the beat-wave is the primary limiting factor in beat-wave amplitude and duration for beat-waves driven by our 350 psec long CO_2 laser[6]. Future beat-wave experiments will avoid this limitation by using a sub 10 psec laser to drive the beat-wave to peak amplitude before ion effects become important.

The first step in obtaining significant energy gains for a relativistic electron beam in a plasma is "trapping" of the externally injected electrons by the plasma wave potential[7]. While trapping is not a necessary condition for energy gain, only trapped electrons can gain the theoretically maximum amount of energy limited by dephasing which occurs when the polarity of the electric field of the plasma wave changes its sign so as to decelerate particles rather than to accelerate them. A trapped electron, by definition, moves synchronously with the wave at the point of reflection in the wave potential. At this point the trapped electron has a relativistic Lorentz factor $\gamma_{ph} = (1 - v_{ph}^2/c^2)^{-1/2}$ where v_{ph} is the phase velocity of the wave. In addition to allowing large energy gains, trapping tends to bunch the electrons in phase space resulting in a relatively narrow energy spread which is necessary for most applications. Trapped electrons bunch in physical space because the trailing electrons see a higher field than the leading electrons and tend to catch up with the latter. This bunching can then lead to a narrow energy spectrum as all the electrons subsequently interact with roughly the same accelerating field. If the initial electron energy is less than the kinetic

3

energy of an electron moving synchronously with the wave, $0.511(\gamma_{ph} - 1)$ MeV, observation of accelerated electrons with energies greater than this is indicative of acceleration of trapped electrons by the wave. The first evidence of such trapped particle acceleration of externally injected electrons by a relativistically propagating plasma wave is presented in Chapter 3 of this thesis[8].

An effect which may limit the amplitude and duration of driven beat-waves is the coupling of the beat-wave to other modes in the plasma which have non-relativistic phase velocities. The modes of primary concern are ion waves driven by stimulated Brillouin scattering (SBS) and electron plasma waves driven by stimulated Raman scattering (SRS). Coupling between the beat-wave and ion waves has been seen in laser-plasma experiments[9] and explained theoretically[10] but coupling between SRS and the beat-wave had not been considered before. As future beat-waves will be driven on time scales shorter than an ion period, SBS will not have time to grow and thus coupling to it will not be an important effect. However, coupling between SRS and the beat-wave will occur. The first experimental evidence of this coupling is shown in Chapter 4. More importantly, it is also shown that this coupling, while affecting the modal structure of the SRS significantly, has little effect on the beat-wave and thus is not a serious concern for future beat-wave experiments[11]. These results may also be important in the quenching of Raman backward scattering by coupling with Raman forward scattering.

The stimulated Raman backscatter instability is important in that it affects both the laser and the plasma in beat-wave experiments. Thus Chapter 5 deals with the evolution of this instability into stimulated Compton scattering through

wave-breaking which involves the trapping and acceleration of background electrons by the large amplitude Raman wave. This trapping, shown in simulations, causes a return current of the untrapped electrons to flow towards the laser to maintain charge neutrality. This return current Doppler shifts the Raman backscatter light leading to a downshift in Raman frequency as the wave wave-breaks and evolves into Compton. This frequency downshift as a signature of Raman wave-breaking is shown both experimentally and in simulations in Chapter 5[12].

As the parameters of the CO_2 laser used to drive the beat-waves and instabilities are important for understanding the experiments, Appendix A explains how the short 350 psec (FWHM) laser pulses are generated via free induction decay and measured using the optical Kerr effect. Also included in this appendix are the measurement of the transverse profile and calculation of v_{osc}/c of the laser. Appendix B deals with driving of the beat-wave, including the derivation of the ponderomotive force used in the PIC code WAVE to replace the high frequency laser fields and thus make it possible to simulate the actual experimental conditions (explained in Chapter 3) and a study of how transverse effects other than plasma expulsion affect the amplitude and usefulness of the beat-wave as an electron accelerator.

Chapter 2

Dynamics of the Resonantly Excited Relativistic Plasma Wave Driven by a CO_2 Laser

2.1   Introduction

In many collective particle acceleration schemes, a relativistically propagating space-charge or plasma wave ($\gamma = (1 - (v_{ph}/c)^2)^{-1/2} \gg 1$) is used for accelerating charged particles [1, 13]. Since the accelerating field of such a wave is directly related to its amplitude, it is important to know the spatial and temporal structure of this wave in order to predict the energy gain or loss by a particle. In the Plasma Beat Wave Accelerator (PBWA) the relativistic plasma wave is resonantly excited by two laser beams beating in a plasma such that their frequency difference $\Delta w = w_0 - w_1$ is approximately equal to the plasma frequency w_p[1, 14]. It is easy to show that if $w_0, w_1 \gg w_p$, then the plasma

wave has a relativistic phase velocity that is equal to the group velocity of the laser, $v_{ph} = v_g = c(1 - w_p^2/w_0^2)^{1/2} \approx c$. In the simplest case, where the the pumps are constant amplitude, monochromatic plane waves and weakly relativistic, $v_{0,1}/c = eE_{0,1}/mw_{0,1}c \ll 1$, the plasma wave grows secularly and saturates due to relativistic detuning[15].

In a real experiment however, the situation is far from the idealized model described above. Typically, a two frequency laser with some finite rise-time is fired into a neutral gas. The laser must first ionize the gas and create a plasma of just the right density to excite the plasma wave resonantly. A focused laser beam will create a plasma of a finite volume via multiphoton or tunneling ionization[16] and once created such a plasma will begin to expand, thus reducing the density. This hydrodynamic expansion coupled with the transverse ponderomotive forces associated with both the laser[17] and the plasma wave itself[18] can greatly modify the dynamics of the plasma wave.

In this chapter we study the temporal dynamics of the beat excited relativistic plasma wave (referred to as the beat-wave) by using frequency and wavenumber resolved Thomson scattering as a diagnostic. The time resolved spectrum, (w, t), shows the fundamental and the second harmonic of the plasma wave whereas the wavenumber resolved spectrum (w, k), also shows the presence of the third harmonic, indicating that large amplitude plasma waves were excited in the experiments. These experimental results represent the most detailed experimental measurements on beat-wave excitation to date.

We first calculate the harmonic content of a relativistic plasma wave as a function of the amplitude of the fundamental. The peak beat wave amplitude is then estimated from the absolute Thomson scattering signal level from the beat-wave

fundamental and confirmed by the ratio of the 2nd harmonic scattering to the fundamental at approximately 33±11%. These results are then compared to 2-D particle in cell code simulations using the experimental parameters which give similar beat-wave amplitudes and pinpoint plasma blowout from the ponderomotive force of the plasma wave as the limiting factor in beat wave amplitude and duration. The transverse fields of the beat wave are probed by time resolving the scattering of a 2 MeV electron beam co-propagating with the CO_2 laser. The effects of plasma blowout can also be seen in the electron scattering measurements, where scattering is reduced for 500 psec immediately after the break-up of the beat-wave, indicating that there is little plasma left on axis which could contain the fields necessary for scattering the electron beam.

2.2 Harmonic Content of a Relativistic Plasma Wave

As the relativistic plasma wave grows, its waveform steepens. This implies that its frequency and wavenumber spectrum contains harmonics of the fundamental (w_p, k_p) and that as the wave continues to grow the harmonic components of the density perturbation increase in amplitude relative to the fundamental. In this section we show that the ratio of the harmonic amplitudes should give a deterministic measure of the amplitude of the relativistic plasma wave. The harmonic amplitudes are somewhat different in the relativistic case compared to those for a non-relativistic plasma wave[19] (e.g., excited by stimulated Raman backscatter) because of additional nonlinearities as will be shown below. The analytical predictions are then shown to be in excellent agreement with the amplitude of the harmonics of the beat-wave based on Hilbert transforms of a numerical integration of the beat-wave equations under the quasi-static approximation[20].

The nonlinear corrections to plasma waves was one of the earliest nonlinear plasma physics topics. Dawson[21] showed that in the absence of relativistic mass corrections a one-dimensional plasma wave oscillates at the plasma frequency, $w_p = \sqrt{4\pi n_0 e^2/m}$, independent of the amplitude of the wave. However, although no nonlinear frequency shifts exist, the waveform steepens for nonlinear plasma waves resulting in harmonic generation. In particular, if the wave is of the form $n_e = n_0 + \sum_{l=1}^{\infty} \delta n_l \cos(l\psi)$ then it can be shown by using the Lagrangian coordinate description[19] that for non-relativistic waves

$$\delta n_l = \frac{l^{l-1}}{(l-1)!2^{l-1}} \delta n_1^l$$

in the $\delta n_1 \ll 1$ limit. Here n_0 is the average plasma density, δn_l are the harmonic components of the density perturbations associated with the wave, and $\psi = kx - wt$ with $w \approx w_p$.

Neglecting relativistic mass corrections is not valid for plasma waves with phase velocities near the speed of light, c. The reason for this is that the fluid velocity in a wave approaches v_{ph} for large amplitudes. It is well known that relativistic corrections cause a nonlinear frequency shift which is $w_{p_{nl}} = w_p(1 - \frac{3}{16}\delta n_1^2)$ in the small amplitude limit[22]. Not surprisingly, the relativistic corrections also alter the harmonic content of the wave.

To calculate the harmonic content of relativistic plasma waves, we begin with the momentum flux equation

$$\frac{\partial}{\partial t}np + \frac{\partial}{\partial x}nvp = -enE \tag{2.1}$$

where the fluid variables in Eq. 2.1, n, p, and E are plasma density, momentum, and electric field respectively. It will be simpler if we choose a set of three fluid variables which are related through linear equations. Therefore, we choose n, J,

9

and E, which are related to each other by the continuity equation and Gauss' law:

$$\frac{\partial}{\partial t}(-en) + \frac{\partial}{\partial x}J = 0; \qquad \frac{\partial}{\partial x}E = 4\pi e(n_0 - n)$$

Rearranging Eq. 2.1 in terms of n, J, and E and normalizing $n \equiv n_0 + \delta n$ to n_0, J to $en_0\mathrm{v}_{ph}$, x to v_{ph}/w_p, t to w_p^{-1}, and E to $m\mathrm{v}_{ph}w_p/e$ gives

$$\frac{\partial}{\partial t}(\gamma J) - \frac{\partial}{\partial x}\frac{\gamma J^2}{n} = nE \tag{2.2}$$

where $\gamma = (1 - (\alpha J/n)^2)^{-1/2}$ with $\alpha = v_{ph}/c$ represents the relativistic mass corrections for high phase velocity waves. Equation 2.2 can be Taylor expanded to fifth order to obtain

$$\frac{\partial}{\partial t}\left\{J + \frac{1}{2}\alpha J^3(1 - 2\delta n + 3\delta n^2) + \frac{3}{8}\alpha^2 J^5\right\} +$$

$$\frac{\partial}{\partial x}\left\{J^2(1 - \delta n + \delta n^2 - \delta n^3) + \frac{1}{2}\alpha J^4(1 - 3\delta n)\right\} = E + \delta nE \tag{2.3}$$

Equation 2.3 can now be used iteratively to generate the harmonic content of plasma waves in the limit that $\delta n \ll 1$. If $\delta n = \sum_{l=1}^{\infty}(\delta n_l/2)e^{il\psi} + c.c.$ then $J_l = -\delta n_l$ and $E_l = (i\delta n_l/l)$. Solving for the harmonics in δn, which is measured by the Thomson scattering in the experiment, gives

$$\delta n_2 = \delta n_1^2, \quad \delta n_3 = \left(\frac{9}{8} - \frac{9}{64}\frac{\mathrm{v}_{ph}^2}{c^2}\right)\delta n_1^3, \quad \delta n_4 = \left(\frac{4}{3} - \frac{3}{8}\frac{\mathrm{v}_{ph}^2}{c^2}\right)\delta n_1^4$$

In the limit that $\mathrm{v}_{ph} \approx c$ these reduce to $\delta n_m = A_m\delta n_1^m$ where $A_1 = 1$, $A_2 = 1$, $A_3 = 63/64$, and $A_4 = 23/24$.

To confirm that these harmonic coefficients are indeed near one, a Runge-Kutta solution to the 1D beat-wave equation under the quasi-static approximation[20, 23], is used to determine the oscillating density of the plasma as a function of time for our experimental parameters. The equation is

$$\frac{\partial^2\phi}{\partial\xi^2} = \frac{w_p^2}{2c^2}\left(\frac{1 + a^2}{(1 + \phi)^2} - 1\right) \tag{2.4}$$
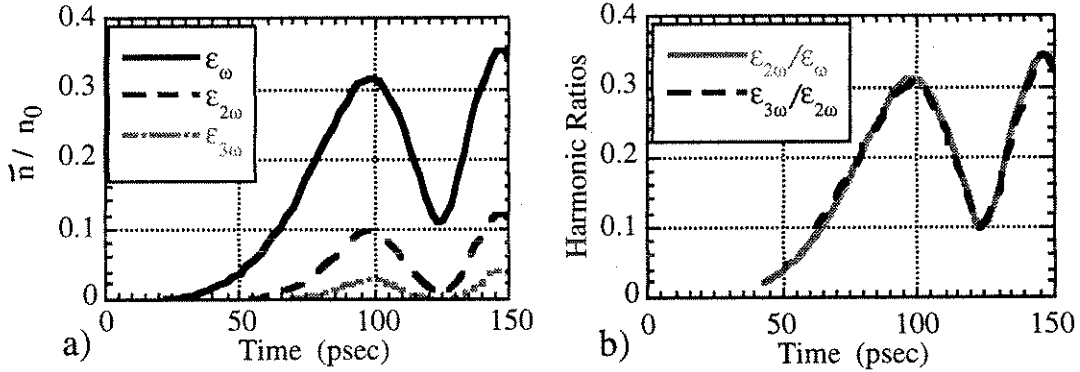
Figure 2.1: Amplitude of harmonics of beat-wave density perturbations based on numerical solution of beat-wave equation. The dip in beat-wave amplitude at 125 psec is caused by relativistic dephasing. a) Amplitude of harmonics. b) Ratio of 3rd harmonic to 2nd and 2nd harmonic to fundamental.

where the density perturbation is given by $\delta n_e/n_o = (c^2/w_p^2)\partial^2\phi/\partial z^2$. Here $\phi = |e|\Phi/mc^2$, $\xi = z - ct$, and $a = |e|\vec{A}/m_0 c^2$ where Φ is the scalar potential of the plasma wave and $\vec{A}$ is the vector potential of the laser. The harmonics of the oscillation are then extracted, where the mth harmonic, $n_m(t)$, consists of the frequency components of the density perturbation in the range $(m - \frac{1}{2})w_p < w < (m + \frac{1}{2})w_p$. The amplitude of each harmonic is calculated as a function of time using a Hilbert transform,

$$\mathcal{H}\{x(t)\} = -\frac{1}{\pi}\int \frac{x(\tau)}{t - \tau}d\tau. \tag{2.5}$$

where if $n_m(t) \equiv \delta n_m \sin(m w_p t + \theta_m)$, then $\delta n_m = (\mathcal{H}\{n_m(t)\}^2 + n_m(t)^2)^{1/2}$. The relationship between the amplitude of the beat-wave and its harmonics is shown in Fig. 2.1 and agrees quite well with the analytic result. The ratios of the 2nd harmonic to the fundamental and the third harmonic to the second harmonic are plotted in Fig. 2.1(b), showing that A_2 and A_3 are approximately equal to 1. The estimate of the harmonic amplitudes based on the simulation is not accurate enough to distinguish between a value of 1 and 63/64 for A_3.

11

2.3 Experimental Set-up

In the experiment, the plasma wave was generated by the ponderomotive force exerted[17] on the plasma electrons by beating two frequencies in a short (≈ 150 psec rise, 300 psec FWHM) intense (70 J, 300 μm diameter ($2w_0$)) CO_2 laser pulse. The CO_2 laser creates the plasma by fully ionizing hydrogen gas via tunneling ionization. By adjusting the H_2 gas pressure, the plasma resonant frequency can be set to the difference frequency between the two laser lines (10.3 μm and 10.6 μm). This occurs at a plasma density of 9.4×10^{15} cm^{-3}. The initial density is set about 10 - 15% higher than resonant density to compensate for plasma blowout by the laser. Thus the plasma should drop to resonant density at approximately the same time as the laser reaches its peak intensity. Some uncertainty in the initial plasma density exists because of nitrogen impurities of up to 5% in the static fill H_2 gas caused by small leaks in the vacuum chamber of the experiment. As four electrons per N_2 molecule are ionized by the CO_2 laser versus only two per H_2 molecule at the peak intensity of the laser, the initial density is only known to within 5%. In addition to increasing the plasma density, these nitrogen molecules will affect the density evolution of the plasma. The second electron from atomic nitrogen ionizes later in the CO_2 pulse than the electron from hydrogen, compensating somewhat for plasma blowout, and the nitrogen ions are much heavier than the hydrogen and thus will not be expelled as easily.

The driven plasma beat-wave has a wavenumber fixed by the difference between the wavenumbers of the two laser lines at $\Delta k = k_1 - k_2 = 1.83 \times 10^{-2}$ μm^{-1} and a diameter of about 220 μm. Images of visible light show the plasma extending over approximately ± 1 cm in the propagation direction of the CO_2 laser, with

an intense region approximately 1 cm long in the middle of the plasma. Based on these images and on a simple model that simulates the plasma formation via tunneling ionization in the Gaussian focal region of the laser we deduce that the plasma is nearly uniform over about 1 cm[16]. The plasma density fluctuations associated with the beat-wave are measured using collective small angle Thomson scattering by a 2ns (FWHM), 50MW, 0.53 μm optical probe beam incident on the plasma at angle of 87° relative to the propagation direction of the CO_2 laser. Both the frequency and wavenumber of the waves in the plasma can be determined as a function of time by this diagnostic as the light scattered by the plasma is shifted by the w and k of the plasma waves [24].

Because of the small k of the beat-wave, a line focus of the probe beam is required both to obtain a good signal to noise ratio and to resolve the k spectrum of the beat-wave harmonics[25]. The k resolution of a spherically focused probe beam is limited by the cone angle of focusing to $2\pi/(\lambda_{pr} f^{\#})$ where λ_{pr} is the wavelength of the probe laser. For our probe laser this would be 0.4 μm^{-1} if it were spherically focused at $f/30$, 25 times larger than the shift in k associated with the beat-wave. For our cylindrically focused probe beam, the quality of the probe beam and optics limits the k resolution in the direction of the beat-wave to 5×10^{-3} μm^{-1}, 80 times better resolution than the spherically focused setup and 3 times smaller than the k shift caused by scattering from the beat-wave.

As shown in Fig. 2.2(a) the Thomson scattering input lenses, S_1 and C_1, focus the beam to a horizontal line focus of length 6 mm and height 100 μm. The output lenses, C_2 and S_2, eliminate the astigmatism in the beam and refocus the unscattered light to a 600 μm spot on a razor blade beam dump. The effective focal length of these two lenses in the horizontal dimension is 60 cm. The angular

13
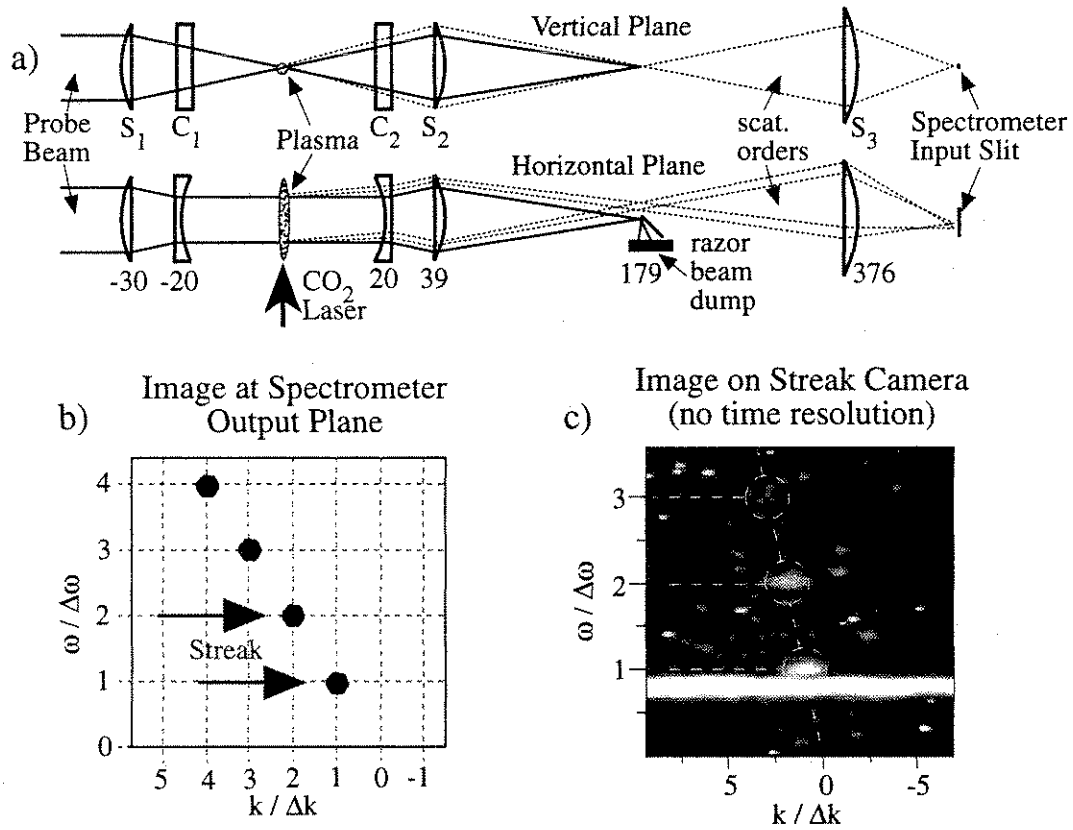
Figure 2.2: Thomson scattering setup. a) Optical setup. Numbers below lenses are the position relative to the plasma in centimeters. Letters (S) and (C) indicate $f = 30$ cm spherical and $f = -20$ cm cylindrical lenses respectively. b) Expected shift in frequency, w, and wavenumber, k of probe light scattered by beat-wave, normalized to the frequency and wavenumber (Δw, Δk) of the beat-wave. Arrows show increasing time when this spectrum is time resolved by the streak camera. c) Actual spectrum seen on streak camera. Broadening in k is caused by 100 psec duration of beat-wave. Bright region at $w/\Delta w \approx 0.8$ is stray light shifted in frequency by Raman scattering in air outside the vacuum chamber.

shift of the scattered light, $\Delta k/k_g$ where $k_g = 2\pi/\lambda_g = 1.18 \times 10^5$ cm^{-1}, is 1.48 mrad which corresponds to a shift of 1.05 mm per harmonic at the razor blade. The razor blade edge is 600 μm in from the center of the main beam, allowing all the harmonics to pass but blocking most of the unscattered stray light. A final lens relays these harmonics onto the entrance slit of an imaging spectrometer that has a prefilter to further reduce the stray light. The harmonics on the entrance slit are about 70 μm in diameter and 190 μm apart.

The spectrometer disperses the harmonics in frequency on the axis perpendicular to the k dispersion while imaging the k spectrum from the slit, producing an w-k spectrum as shown in Fig. 2.2(b). A streak camera with no entrance slit is then placed at the output plane of the spectrometer with time on the same axis as k. On a slow sweep speed (1 ns / mm), the camera has minimal time resolution and simply takes a picture of the w-k spectrum[24] of the beat-wave harmonics. The fact that the w-k, t Thomson scattering works as expected is shown in the beat-wave shot of Fig. 2.2(c). On a fast sweep speed (100 ps / mm), the camera will produce time resolved amplitude and frequency measurements of the beat-wave and its harmonics, with a slight shift in the onset of each harmonic due to the shift in k evident in Fig. 2.2(c).

2.4   K-matching for relativistic plasma waves

The k spectrum of a plasma density perturbation is given by its spatial Fourier transform. The beat-wave, being about 1 cm long, has a very narrow k spectrum in the longitudinal direction which can be approximated as a delta function. However, as it is only about 220 μm across, its transverse k spectrum is broad, and must be taken into account when calculating absolute scattering efficiencies

which are necessary for estimating the beat-wave amplitude.

As the beat-wave amplitude is proportional to first order to the CO_2 laser intensity until saturation of the wave[15], we can calculate the k-spectrum of the beat-wave based on the k spectrum of the CO_2 laser. The $f/11.5$ focusing optics of the CO_2 would produce a Gaussian focal spot of size $w_0 = 80$ μm for a laser with a Gaussian, transform limited profile. The transverse k spectrum of this spot would be $\mathcal{F}_y\{\delta n_1 \exp[-2(y/w_0)^2]\} = w_0 \delta n_1 \sqrt{\pi/2} \exp(-w_0^2 k_y^2/8)$. However, the actual measured spot size, w_1, is 150 μm (best fit Gaussian) because the laser beam at the focusing mirror is not quite Gaussian. The transverse profile of the focal spot is also more flat-topped than a Gaussian, but a Gaussian is assumed for simplicity. Although the spot is larger, the k spectrum of the fields of the laser beams is still given by the $f^{\#}$ of the optics and the spatial bandwidth of the beat-wave should be approximately that of the transform limited beam, $\exp(-w_0^2 k_y^2/8)$.

Given the bandwidth of the transverse spectrum and the spot size of the beat-wave, the approximate spectral amplitude and profile can be estimated either through Parseval's theorem which states that the integrated intensity be equal in real and frequency space or by taking the Fourier transform after adding a phase variation term Γ to the beat-wave to increase its bandwidth without changing its width. In either case, the spectrum is given by:

$$\xi_1(k_y) = \mathcal{F}_y\{\exp[-2\Gamma(y/w_1)^2]\} = \sqrt{\frac{w_0 w_1 \pi}{2}} \exp\left(-\frac{\Gamma^* w_0^2 k_y^2}{8}\right) \qquad (2.6)$$

where $\Gamma = 1 - j[(w_1/w_0)^2 - 1]^{1/2}$ is the phase term. The phase and amplitude variations in the fields across the 150 μm spot which broaden the bandwidth may cancel somewhat in the beat-wave if the variations in phase of the two laser lines are correlated, reducing the bandwidth slightly below the estimate based

16

on the f number of the focusing optics. As can be seen by varying w_0 in Eq. 2.6, the decrease in bandwidth would increase the amount of scattering for near perfect k-matching $(k_y < \sqrt{2}/\text{w}_0)$ but decrease it for less perfect k-matching $(k_y > \sqrt{2}/\text{w}_0)$. As the Thomson set-up described later involves a k-mismatch of $k_y = \Delta k = 0.0183~\mu\text{m}^{-1}$ which is greater than $\sqrt{2}/\text{w}_0 = 0.0177~\mu\text{m}^{-1}$, the lower bandwidth would lead to a decrease in scattered signal for a given beat-wave amplitude and thus an underestimate of the beat-wave amplitude. On the other hand, non-linear dephasing of the beat-wave caused by relativistic effects may increase the bandwidth of the beat-wave, leading to an overestimate of the beat-wave amplitude. As the scattering efficiency is a function of bandwidth for all k_y, this uncertainty would exist even if the Thomson scattering were perfectly k-matched.

In Sect. II, it was shown that the amplitude of the mth harmonic of the beat-wave is proportional to the fundamental to the mth power, $\delta n_m \propto \delta n_1^m$. Therefore the transverse k-spectrum of the mth harmonic is:

$$\xi_m(k_y) = \mathcal{F}_y\{\exp[-2\Gamma m(y/\text{w}_1)^2]\} = \sqrt{\frac{\text{w}_0\text{w}_1\pi}{2m}}\exp\left(\frac{-\Gamma^*\text{w}_0^2 k_y^2}{8m}\right) \qquad (2.7)$$

The k-matching equations for scattering off the beat-wave with a probe laser beam are:

$$k_i\cos(\theta_i) = \Delta k + k_s\cos(\theta_s) \qquad\qquad k_i\sin(\theta_i) = k_y + k_s\sin(\theta_s) \qquad (2.8)$$

where k_i and k_s are the wavenumbers of the probe and scattered beams, θ_i and θ_s are the incident and scattering angles, $\Delta k = 0.01825~\mu\text{m}^{-1}$ is the beat-wave wavenumber, and k_y is the transverse k mismatch.

The Bragg input and scattering angles, θ_i and θ_s, required to eliminate the k mismatch for the fundamental can be calculated from Eq. 2.8 as $\theta_i \approx \theta_s = 30$
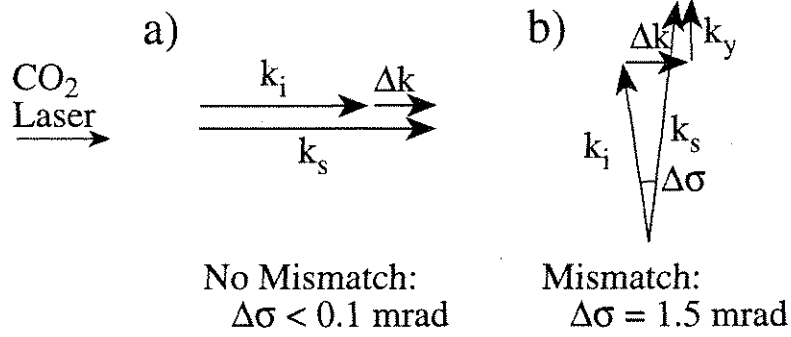
Figure 2.3: Thomson Scattering k mismatch

mrads. This angle is difficult to use both because the input beam is within the f number of the CO_2 optics and because the change in angle, $\Delta\theta = \theta_s - \theta_i = 0.05$ mrads, is too small to separate the scattered beam from the probe beam which is at least six orders of magnitude more intense (Fig. 2.3). In our experiment the probe beam (frequency doubled yag laser) is sent nearly perpendicular to the CO_2 beam to eliminate these difficulties. For this case, the incident and scattering angle and transverse k mismatch for the fundamental and harmonics are:

$$\theta_i = \frac{\pi}{2} \text{ rad} \qquad \theta_s = \frac{\pi}{2} + m \times 0.00155 \text{ rad} \qquad k_y = m\Delta k \qquad (2.9)$$

For this mismatch, $\xi_m = 1.25 \times 0.765^m \sqrt{w_0 w_1/m}$. The ratio of scattered power from the mth harmonic of the beat-wave to incident power is given by the Bragg scattering formula

$$P_m/P_i = \frac{\Psi_m}{4} \left[A_m \delta n_1^m n_0 r_0 \lambda_{pr} \xi_m\right]^2 \qquad (2.10)$$

where $r_0 = 2.82 \times 10^{-13}$ cm is the electron radius and ξ_m can be thought of as an effective scattering length[26]. For our experiment, the probe wavelength λ_{pr} is 0.532 μm, the plasma density n_0 is 9.41×10^{15} cm^{-3}, and the probe power P_i is approximately 50 MW. The factor Ψ_m takes into account the overlap between

18

the probe beam and the mth harmonic of the beat-wave in the vertical direction. It is equal to the integral of the incident vertical intensity distribution multiplied by the square of normalized amplitude of the mth harmonic of the beat-wave.

$$\Psi_m = \int \frac{\exp\left[-2(y/\mathrm{w}_2)^2\right]}{\mathrm{w}_2\sqrt{2\pi}} \exp\left[-4m(y/\mathrm{w}_1)^2\right] dy = \left(1 + \frac{2m\mathrm{w}_2^2}{\mathrm{w}_1^2}\right)^{-1/2} \quad (2.11)$$

Here $\mathrm{w}_2 = 100$ μm is the spot size of the probe laser in the vertical direction. Thus, it is possible to directly calculate the beat-wave amplitude as a function of time given the ratio of scattered to incident probe power and Eq. 2.10.

2.5 Time Resolved Measurements of the Beat-Wave Harmonics

As shown in Fig. 2.4(a), the intensity of probe light scattered from the fundamental and 2nd harmonic of the beat-wave was measured on a streak camera with a sweep speed of 100 ps/mm, providing a temporal resolution of 10 psec. The speckle of noise across the image was caused by background x-rays. The spectral width of scattering from the beat-wave is instrument limited at 0.1 Δw. The downward shift in frequency of the fundamental and 2nd harmonic of approximately 10% over 100 psec is too large to be explained by relativistic frequency shift $w_{p_{nl}} = w_p(1 - \frac{9}{64}\delta n_1^2) = 0.99 w_p$[22] and thus strongly suggests a decrease in plasma density due to blowout of the plasma in the transverse direction at the rate of approximately 20% over 100 psec. The 2nd harmonic is shifted earlier by 12 psec relative to the fundamental because of the difference in k as explained earlier (see Fig. 2.2(c)). The power scattered from the fundamental is normalized to the incident power of the probe laser and plotted in Fig. 2.4 (b). The intensity of the probe light is measured by removing the razor blade beam dump

19
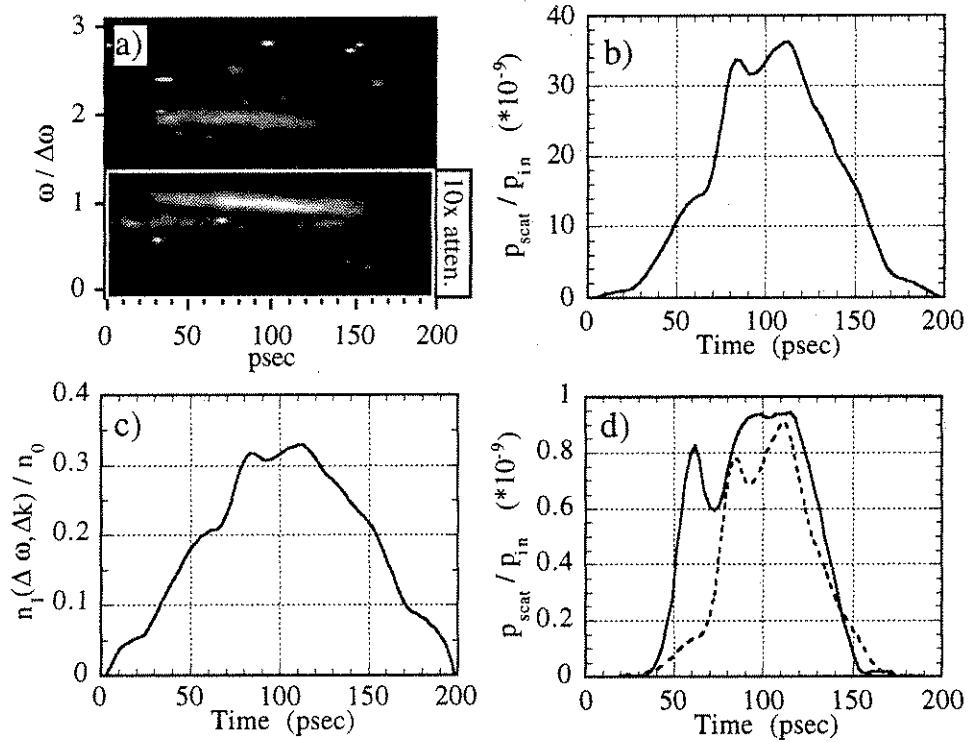
Figure 2.4: Thomson scattering signal. a) Time resolved spectrum of Thomson scattered light showing scattering from fundamental and 2nd harmonic of beat-wave. Stray light at 0.8 Δw and beat-wave fundamental are attenuated by a factor of 10. b) Ratio of spatially integrated scattered light from fundamental to incident probe light vs time. c) Beat-wave amplitude as a function of time based on scattered light from fundamental shown in Fig 2.4(b). d) Solid line - ratio of spatially integrated scattered light from second harmonic to incident probe light. Dotted line - expected scattered light signal based on beat-wave amplitude shown in Fig 2.4(c) and harmonic theory.

shown in Fig. 2.2(a), adjusting the spectrometer pre-filter to pass the probe laser frequency, and streaking the probe at 100 ps/mm with appropriate attenuation in the beam path.

Based on the ratio of light scattered from the fundamental to the incident probe light, Fig. 2.4(b), the beat-wave amplitude as a function of time is estimated using Eq. 2.10 and plotted in Fig. 2.4(c). The important features to note are a peak amplitude of $\delta n_1 = 33\%$ and a duration of 100 psec (FWHM). Based on the Bragg scattering formula (Eq. 2.10) and the theoretical relationship between the second harmonic and the fundamental $\delta n_2 = \delta n_1^2$, the expected scattering from the second harmonic of the beat-wave can be calculated. This estimate, shown as the dashed curve in Fig. 2.4(d), matches the actual scattering level also shown in Fig. 2.4(d) well, confirming the beat-wave amplitude estimate of 33%. The timing of the second harmonic in Fig. 2.4(d) relative to the fundamental has been adjusted for the shift in k. The spike at 60 psecs in Fig. 2.4(d) is probably due to an x-ray as it does not match the temporal profile of the fundamental. Even though the two estimates of beat-wave amplitude agree, the assumptions about the beat-wave transverse profile and bandwidth in Sect. IV limit the accuracy of the estimates to within about a factor of 2. Thus we conclude that the beat-wave amplitude is between 22% and 44% based on the Thomson scattering.

2.6 Simulations

The maximum amplitude for a resonantly driven beat-wave oscillation according to the Rosenbluth & Liu limit is $\delta n = (16a_1a_2/3)^{1/3}$[15]. Here $a_{1,2} = eE_{1,2}/mw_{1,2}c$ where E_1 and E_2 are the electric field amplitudes of the two co-propagating laser

frequencies. For our experimental conditions, a_1 and a_2 are 0.13 and 0.18 respectively, giving a peak estimated amplitude of 50%, significantly larger than the experimental results. However, this limit overestimates the beat-wave amplitude because of two assumptions which are not valid for most experiments. These assumptions are instantaneous rise time of the laser and no transverse effects or expulsion of the plasma by the ponderomotive force of the laser and beat-wave.

The effect of the rise-time of the laser can be included by integrating over the laser pulse using Eq. 2.4 as described in Sect. II, producing a reduced estimate of the peak amplitude of the beat-wave of 35% as shown in Fig. 2.1. The oscillation in the amplitude of the beat-wave during the rise-time of the laser in this figure is caused by dephasing between the laser driving force and the beat-wave as the resonant frequency of the plasma is reduced by the relativistic mass increase of the oscillating electrons. This estimate of the maximum amplitude of the beat-wave matches the experimental results well.

However, expulsion of the plasma by the ponderomotive force of the laser[17] and the beat-wave itself[18] also limits the beat-wave amplitude and duration, but is not taken into account by the 1D simulation described in Sect. II. The density reduction caused by the expulsion of electrons before any movement of the ions is small ($\approx 0.4\%$) but the large electric fields generated by the charge imbalance (equal to the average ponderomotive force) cause the ions to accelerate outwards, leading to significant reductions in plasma density. As the plasma density drops, the plasma frequency goes out of resonance with the laser driver, reducing the peak obtainable beat-wave amplitudes. As this is an intrinsically non-linear process, it is very difficult to analyze analytically and simulations must be used.

The beat-wave is modelled self-consistently, including the effects of plasma blowout by the laser and the beat-wave, using a modified version of the fully relativistic 2D PIC code WAVE[27]. The unmodified version of WAVE resolves the high frequency and short wavelength of the laser fields. For the experimental conditions where $w_0/w_p = 30$, resolving both the plasma frequency and the laser frequency is not possible. However, in the experiment, the lasers do not evolve during the transit through the plasma. Therefore, we replace the full laser fields with their ponderomotive force averaged over a laser cycle:

$$F_{p_x} = -\hat{x}\frac{m}{2}\exp\left(\frac{-2y^2}{w_1^2}\right)a_1(t)a_2(t)\Delta k\sin(\Delta wt - \Delta kx) \qquad (2.12)$$

$$F_{p_y} = \hat{y}\frac{m}{2}\exp\left(\frac{-2y^2}{w_1^2}\right)\frac{4y}{w_1^2}\left[\frac{1}{2}(a_1^2(t) + a_2^2(t)) + a_1(t)a_2(t)\cos(\Delta wt - \Delta kx)\right]. \qquad (2.13)$$

Here Δw and Δk are the difference in frequency and wavenumber of the two laser lines, $w_1 = 150\ \mu$m is the spot size of the laser, and m is the electron mass. This force oscillates at the difference in frequency between the two lasers ($\Delta w = w_1 - w_2 \approx w_p$) instead of the laser frequency ($w_0 \approx 34w_p$). With this modification, WAVE only needs to resolve out to the third harmonic of the beat-wave ($3w_p$) rather than the frequency of the laser. It eliminats the physics associated with plasma modes near $2k_0$ of the laser such as stimulated Raman and Brillouin scattering, but still models the beat-wave amplitude accurately as confirmed by benchmarking the new version with the original code using a small frequency ratio w_0/w_p of 5. Effects of the beat-wave on the laser, which are also neglected, should be minimal as the plasma is very underdense ($n/n_{crit} \sim 10^{-3}$) and the interaction is much less than the pump depletion length.

In Fig. 2.5, we show a typical simulation of the experimental conditions. It

consists of a laser pulse with a 100 psec rise-time containing two wavelengths $\lambda_1 = 10.3$ μm, $\lambda_2 = 10.6$ μm with a peak v_{osc}/c of 0.13 and 0.18 respectively. This pulse enters an underdense plasma whose density is chosen such that the laser frequency difference $\Delta w = w_1 - w_2$ is slightly below resonance for the initial plasma density $(n_{init}/n_{res} = 1.074)$.

As shown in Fig. 2.5(a), the plasma density on axis slowly decreases due to the ponderomotive force of the laser until it reaches resonant density at 110 psec. As the plasma approaches resonant density, the beat-wave amplitude, shown in Figs. 2.5 (b) and (c) begins to grow rapidly, reaching a peak of 25% at 120 psec. The ponderomotive force of the beat-wave expels the plasma as seen by the more rapid drop of plasma density with time beyond 110 psec shown in Fig. 2.5(a). This rapid radial expulsion of the plasma casues outward propagating x-type shock waves as seen in Fig. 2.5(d)[28]. The density at the shock front can reach 2.5 times resonant density. As the plasma density drops below resonance, the beat-wave decouples from the driving force of the laser and decays over 40 psecs even though the laser is still present as indicated in Fig. 2.5(c). The plasma wave is again driven to a few percent amplitude around 200 psec in the laser pulse as the expelled plasma rushes back in when the ponderomotive force associated with the earlier large amplitude beat wave disappears. This low level ($\approx$ 5%) plasma oscillation lasts for about 50 psecs in the simulation. As we shall see later, the transverse forces associated with this can be diagnosed by injecting a relativistic beam of electrons into the plasma and measuring the scattering of the electron beam.

Although the peak amplitude of the beat-wave in the simulation (25%) is in reasonable agreement with that of the actual experiment (22% to 44%), the 40
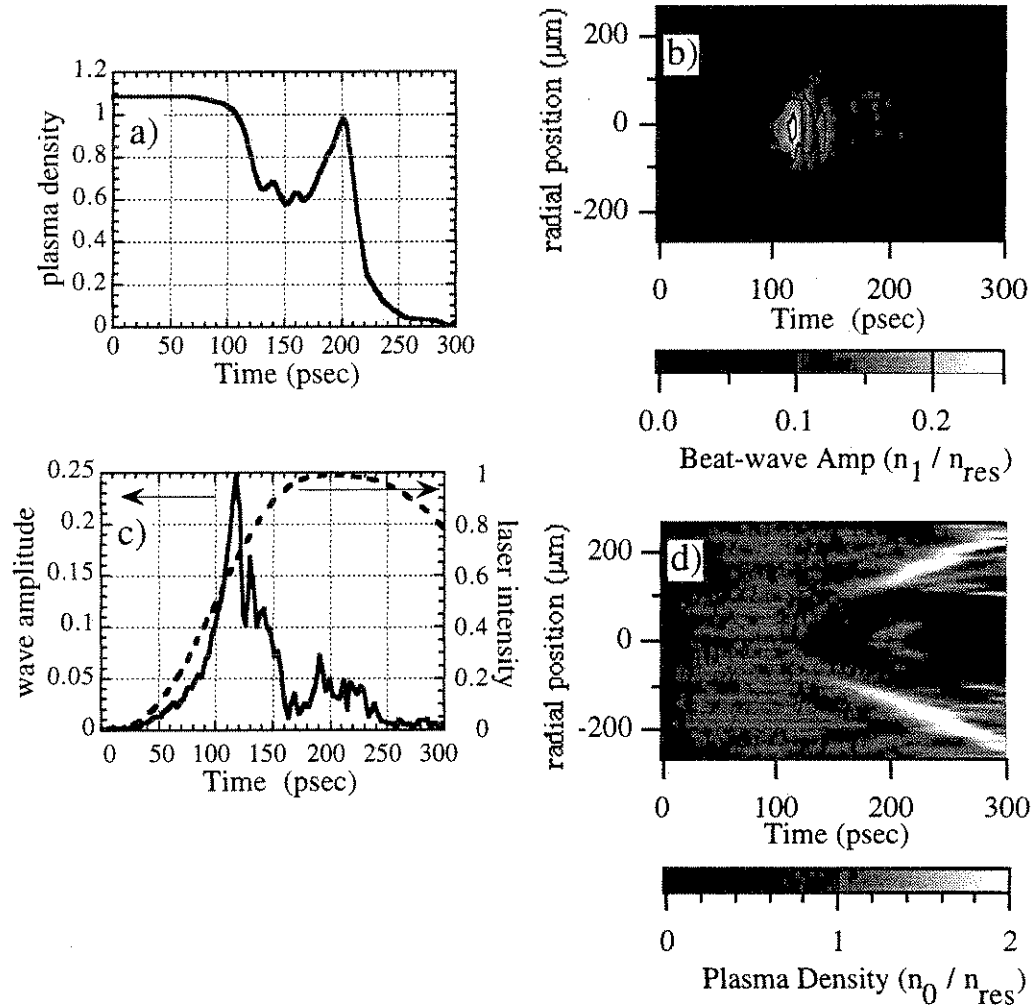
Figure 2.5: Simulation showing evolution of plasma density and beat-wave amplitude at focus. a) Evolution of plasma density on axis. b) Time evolution of beat-wave amplitude as a function of transverse position. c) On axis amplitudes of beat-wave from (b) (solid line) and laser (dashed line) as a function of time. d) Time evolution of plasma density as a function of transverse position from which (a) was taken.

psec duration in the simulation is less than half that of the actual beat-wave. The difference between the simulation and experiment is that in the simulation the density decreases on axis by 30% over 30 psec during the beat-wave while in the experiment the density drops by only 20% in 100 psec.
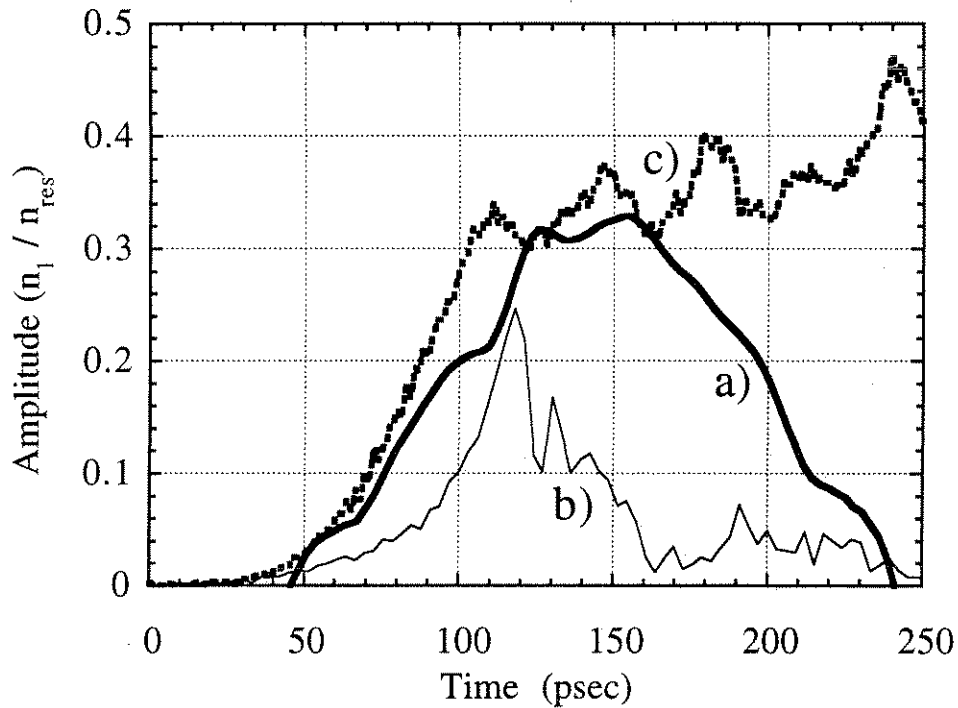
Figure 2.6: Comparison of beat-wave amplitude from experiment and 2D PIC simulation results. a) Experimental estimate of amplitude based on Thomson scattering from fundamental. b) Amplitude on axis from PIC simulation with mobile ions c) Amplitude on axis from PIC simulation with immobile ions

To determine how much the plasma blowout affects the beat-wave duration and amplitude, a 2-D WAVE simulation of the beat-wave was also run using the same parameters as the run shown in Fig 2.5(a), with fixed ions at resonant density. This run produced a peak beat-wave amplitude of between 35% and 40%

with a duration longer than the experimental results. In Fig. 2.6, we show a comparison between the beat-wave estimates based on the Thomson scattering from the experiment and on the PIC simulations with and without plasma blowout. The experimental results are bracketed by the two simulations in both beat-wave amplitude and duration, showing once again that plasma blowout is occuring in the experiment, but at a slower rate than indicated by the simulation.

There are two reasons why the experimentally inferred rate of density decrease may be slower than that seen in the 2D, mobile ions simulations. The first is the heavy nitrogen ion impurity mentioned earlier and the second is the non-Gaussian focused laser intensity profile in the experiments. The latter in particular can inhibit the plasma expulsion rate from the beam center, where the intensity gradients are low, until the plasma is etched away from the edges. Despite these issues, there is a qualitative agreement between the simulation and the experiments, particularly as far as the rise-time of the beat-wave is concerned, and the saturation amplitude in the experiments is reasonably close to the values obtained in the simulations with both mobile and immobile ions.

The static and oscillating components of the transverse electromagnetic fields associated with the beat-wave as a function of time, shown in Figure 2.7, are also obtained from the simulations with mobile ions. Fig. 2.7(a) shows the oscillating radial electric field which as expected has about the same duration as the longitudinal electric field shown in Fig. 2.5(b). Note also that for the experimental spot size the transverse E_y field is only a factor of two less than E_x. As the coherent plasma oscillation breaks up, the plasma electrons are heated up substantially. In the simulations with mobile ions, the initial electron temperature was 26 eV. However when the beat-wave with 25% peak density modulation
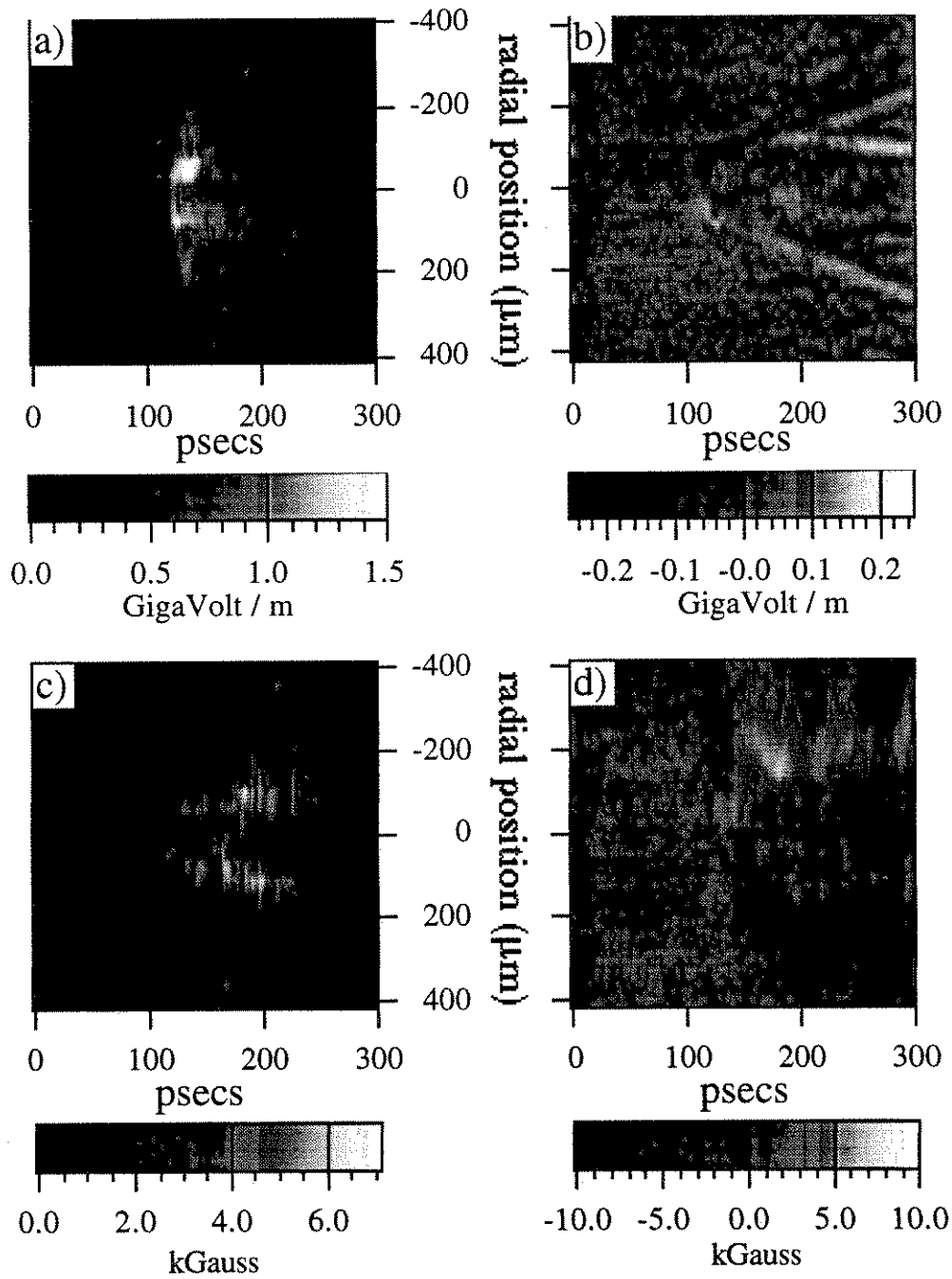
Figure 2.7: Transverse E-M fields associated with Beat-wave. a) Oscillating radial electric field. b) DC radial electric field. c) Oscillating azimuthal magnetic field. d) DC azimuthal magnetic field

28

disrupted the plasma, the electrons heated up to 3 keV. We have experimentally inferred this beat-wave heating of the plasma by measuring the x-ray spectrum in the 2-10 keV range using an x-ray charge coupled device (CCD). The slope of the x-ray spectrum on the laser shots with a large beat-wave was indeed in the 3 keV range. These results will be reported elsewhere[29].

A shock wave that propagates radially outwards is set up as the plasma is expelled by the combined action of the laser and the plasma wave discussed earlier. The density jump across the shock wave is roughly a factor of 2.5. Associated with the density spikes are transverse DC electric fields shown in Fig. 2.7(b) which reach a peak magnitude of around 0.1 GeV/m, about an order of magnitude smaller than the oscillating radial field of the beat-wave. There is also both an oscillating azimuthal magnetic field and a DC azimuthal magnetic field in the plasma. These fields are shown in Fig. 2.7 (c) and (d), respectively. They can reach a peak ampitude of around 10 kGauss.

2.7 Experimental Electron Scattering Measurements

The transverse dynamics of the beat-wave are probed experimentally by sending an electron beam through the plasma collinearly with the beat-wave and monitoring the scattering or deflection of the electron beam by the transverse (azimuthal) electric (magnetic) field. This is done in the following manner: A 2 MeV, 1.5 ns (FWHM) electron beam containing sub 10 psec micropulses, each separated by 110 psec, is injected collinearly with the laser beam. One of the micropulses is primarily accelerated up to 30 MeV and decelerated up to 1 MeV by the longitudinal field of the plasma wave[8]. However the rest of the micropulses can be used to diagnose the transverse electric and magnetic fields in the plasma following the

29

This is consistent with our measurements of the laser pulsewidth of approximately 300 psec (FWHM). When the gas is introduced, such that a *single frequency* laser beam tunnel ionizes the gas and produces a plasma, the electron beam transmission through this resultant plasma is not significantly different than when there is no plasma. However, when a two frequency laser beam drives a beat-wave, the electron transmission through the plasma is affected a great deal. This is shown in Fig. 2.8(c). There are two new features to the electron transmission when the beat-wave is present. First, the smearing of the electrons coincident with the laser pulse is now much stronger and lasts 800 psec when the beat-wave is present compared to only 400 psec when only the laser is present. By comparison with the simulations we believe that the strong scattering of the electrons between zero and 0.8 nsec in Fig. 2.8(c) is due primarily to the transverse AC electric fields in the plasma (Fig. 2.7(a)). Between 0.8 nsec and 1.0 nsec the transmission recovers somewhat (i.e. - the smearing of the electrons is reduced) as the plasma is expelled and the plasma density becomes very low on the axis after the complete disruption of the beat-wave. As there is little plasma on axis, the electric and magnetic fields in this region of the plasma are small and the electron beam is able to propagate with much reduced scattering. Unfortunately the simulations are only run up to 300 psec because of computer-time considerations, preventing us from following the details of the evolution of the density and temperature of the plasma beyond this point. Clearly one expects the plasma to eventually return to the evacuated axial region after the laser pulse is no longer present to maintain the pressure balance. In fact after 1.0 nsec the electron beam is completely deflected as seen by the lack of Cherenkov light indicating that the plasma has returned and some other phenomenon is at work that produces a

large enough magnetic field to deflect the beam by more than 50 mrad.

The duration of this field which develops later in the plasma and deflects the electron beam was measured to be about 5 nsec by varying the timing between the electron beam and the CO_2 laser. To determine whether this scattering field was electric or magnetic, a flourescer which produced a time integrated image of the electron beam was placed in the beam dump. The flourescer showed that the electron beam, when fired a few nsec after the CO_2 laser, was deflected to one side instead of being smeared out by the fields in the plasma. This indicates the presence of a DC magnetic field rather than electric fields which vary on either the electron or ion time scales and thus would smear out the deflection. The deflection on the order of 50 mrad over 1 cm would require a magnetic field of over 400 Gauss. As the initial fields immediately after the beat-wave were between 5 and 10 kGauss, it is unclear whether the magnetic fields late in time are the remnants of the initial fields, or are generated by the growth of the Weibel instability[31] in the anisotropic plasma left by the beat-wave. This is currently being investigated further.

2.8 Conclusions

The dynamics of the relativistic plasma wave resonantly excited by a two frequency laser pulse are studied through experiments and supporting simulations. The plasma wave and its second harmonic were time resolved using a Thomson scattering diagnostic producing an estimate of peak beat-wave amplitude of between 22% and 44%. The theoretical harmonic content for a 1D relativistic wave was determined analytically and checked numerically. The plasma wave amplitude and lifetime are deduced to be limited by plasma blowout which occurs

because of plasma expansion due to pressure gradients and to the ponderomotive forces of the laser and the plasma wave. The effects of this plasma blowout are also seen in the reduction of scattering of the electron beam by the electric and magnetic fields remaining in the plasma immediately after the break-up of the beat-wave and the later increase in scattering as the plasma returns. In the next chapter, these beat-waves are used to trap and accelerate electrons from the 2 MeV relativistic electron beam up to 30 MeV over approximately one centimeter. This level of acceleration requires a beat-wave amplitude of approximately 30%, in good agreement with the Thomson scattering measurements of this chapter.

Chapter 3

Demonstration of Trapped Electron Acceleration by a Laser-Driven Relativistic Plasma Wave

3.1 Introduction

There has recently been a great deal of research into various advanced particle-accelerator concepts[13], the goal of which is to find technologies that push the acceleration rate beyond the roughly 100 MeV/m limit (imposed by RF breakdown) found in conventional accelerating structures. By thus reducing the size, one hopes to bring ultrahigh energy accelerators into practicality or to shrink the cost of more modest-energy accelerators. Relativistic plasma waves, having

phase velocities very close to the speed of light, have been proposed as ultrahigh-gradient accelerating structures[32, 1, 33, 34] for charged particles. In Plasma Beat Wave Accelerator[14] experiments described in this chapter, such plasma waves have been excited in a hydrogen plasma by beating two collinear laser beams whose difference-frequency matches the resonant plasma frequency. A detailed description of these beat-wave experiments is given in the previous chapter. This description includes details of the Thomson scattering diagnostic for measuring the beat-wave amplitude and evolution, 2D one-to-one particle-in-cell (PIC) code simulations of the beat-wave including ponderomotive blow-out, and measurements of the interaction of the injected relativistic electron beam with the transverse electromagnetic fields in the plasma associated with the growth and break-up of the beat-wave. Electrons with an energy of 2 MeV were injected into the plasma wave and the energy spectrum of the exiting electrons analyzed. Accelerated electrons with velocities greater than the phase velocity of the wave conclusively demonstrated trapped particle acceleration. The maximum energy gain of 28 MeV was also consistent with the integrated product of electric field and length inferred independently through optical Thomson scattering.

Relativistic plasma waves are particularly useful for accelerating particles for two reasons. First, the electric fields within these waves can be extremely high. Secondly, the fact that these waves can be made to move at the same speed as a highly relativistic particle means that the accelerating particles will interact with the fields for a long time and can thus be accelerated to very high energies. In this Plasma Beat Wave Accelerator experiment, such a wave is driven by illuminating a suitable plasma with two laser beams of slightly different frequencies. The interference, or beating, of the two beams exerts a force on the plasma at
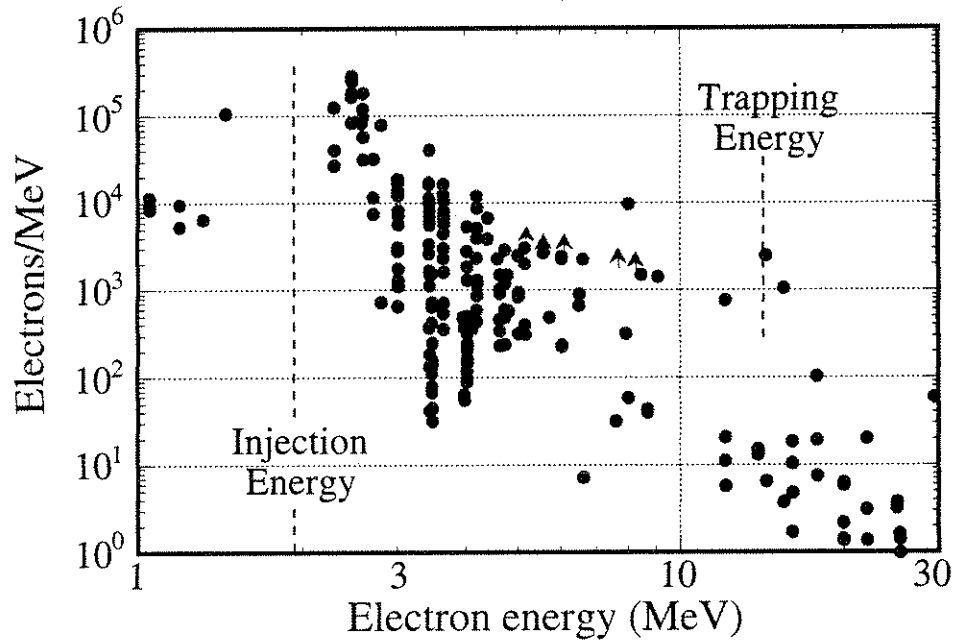
Figure 3.1: The cumulative energy spectrum of electrons exiting the plasma wave within a full cone angle of 6°. For this data, various charge-sensitive preamplifiers and thick lead apertures were used to extend the dynamic range of the electron detectors to over 4 orders of magnitude in electron flux beginning with single-electron sensitivity. The energy dispersion across the aperture of the detector was considered in arriving at the plotted electrons per MeV. The points with arrows are lower bounds due to detector saturation. At a given setting of the electron spectrometer magnetic field, electron data can only be obtained at three energies per laser shot. Therefore, a complete electron spectrum has to be accumulated over many shots. The dashed lines mark the injection energy and the trapping energy where the latter refers to the energy which the electrons must have to move synchronously with the wave.
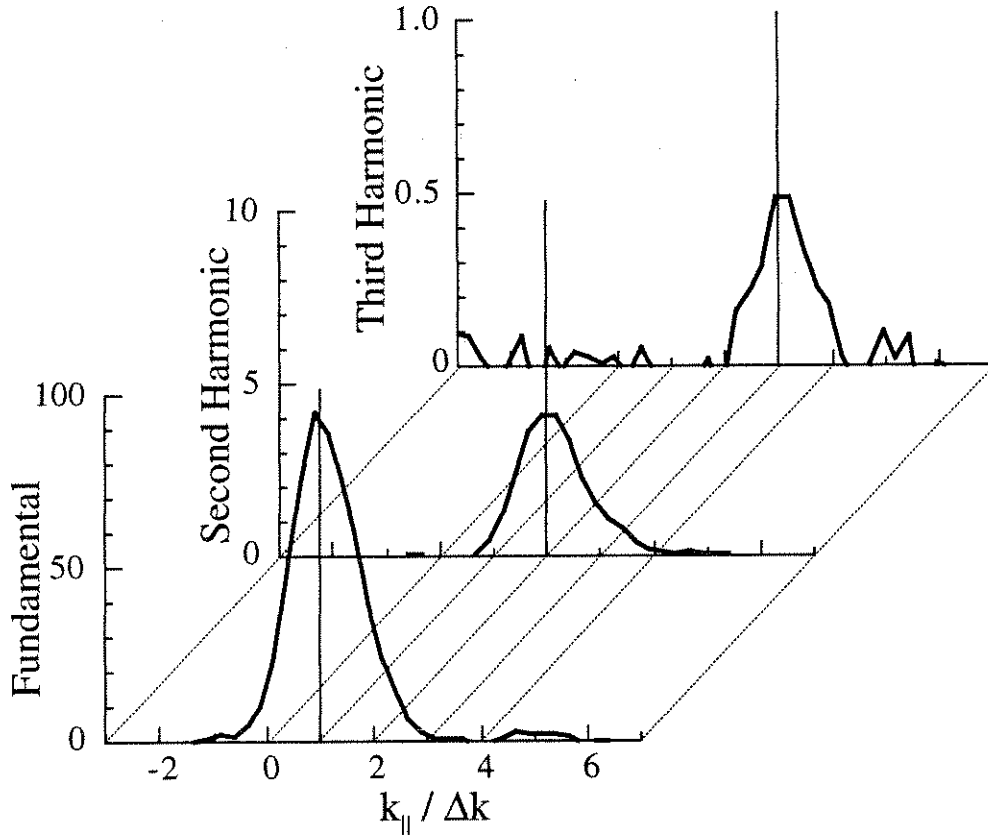
Figure 3.2: Lineouts taken at Δw, $2\Delta w$, and $3\Delta w$ of the time-integrated frequency-wavenumber spectrum of the plasma wave obtained by small-angle Thomson scattering. The width of each peak is instrument limited. In the 90° scattering geometry, energy and momentum ca n only be conserved for photons that scatter from the component of the wave with $k_\perp = k_{||}$ ($= m\Delta k$ for the mth harmonic scattered order). Because the wavelength of the plasma wave and its radial extent are comparable, the plasma wave has a broad perpendicular wavenumber ($k_\perp$) spectrum. From knowledge of the laser spot profile, we can estimate the $k_\perp$ spectrum and thereby quantify the relative amplitude of each wave harmonic.

41

the wave electric fields independent of the energy gain measurement. Essentially, the density perturbations look like a moving volume grating which can diffract the probe beam into frequency-shifted "orders". The 2 ns (FWHM), 50 MW, 0.53 μm optical probe beam (w_{pr}, k_{pr}) traverses the plasma wave at a right angle to its direction of propagation. In this configuration, the probe beam has a cylindrical focus 6 mm (about 20 plasma wavelengths) in length. The scattered light is observed to be at various discrete angles $\theta = k_{||}/k_{pr}$ (where $k_{||} = m\Delta k$), and frequency shifted by $w_{pr} - mw_p$. Here $k_{||}$ is the wavenumber of the plasma wave along the propagation direction of the electron beam and m is an integer number corresponding to the harmonic number of the plasma wave. This beat-excited plasma wave has $k_{||} = \Delta k$ where Δk is the wavenumber difference between the two laser beams. Figure 3.2 shows three lineouts of the time-integrated $w - k$ spectrum of the density perturbations of the wave obtained by the Thomson scattering diagnostic. This spectrum clearly shows discrete peaks at $(m\Delta w, m\Delta k)$ for $1 \leq m \leq 3$ corresponding to scattering of light from the fundamental, second, and third harmonics of the relativistic plasma wave. Using nonlinear wave theory[19], which gives the normalized amplitude of the mth harmonic a_m as a function of the normalized amplitude of the fundamental a_o as $a_m \approx a_0^m$, one can obtain an estimate of the plasma wave amplitude based on its harmonic content. After correcting for the finite-$k_\perp$ effects[38, 25], we obtain an estimate for the density perturbation of 38% of the background density based on the second harmonic to fundamental ratio or 40% from the third to fundamental harmonic ratio. Alternatively, we can obtain an amplitude estimate based on the absolute intensity of the scattered light from which we infer a 30% wave amplitude. This latter estimate agrees well with two-dimensional "particle-in-cell" computer

simulation of our exact experimental parameters. We can compare these optical measurements to the electron measurements by noting that the interaction length for our focusing conditions is expected to be about 1.0 cm[30]. Thus, the 30 MeV electrons gained energy at a rate of 2.8 GeV/m which, from Gauss' Law, corresponds to a wave amplitude of 28%, in good agreement with the independent optical diagnostic and the computer simulation.

3.4 Conclusion

Trapping and acceleration of an electron beam by a plasma beat-wave has been shown, resulting in acceleration of 28 MeV over approximately 1 cm. This acceleration gradient of 2.8 GeV/m is more than 100 times the practical limit for conventional RF accelerators of about 17 MeV/m, but the interaction length of only 1 cm seriously limits the practicality of these accelerators. Energy gains up to 1 GeV should be obtainable with current technolgy using 1 μm lasers and longer interaction lengths. However, for energy gains much above this, it will probably be necessary to use staging of several such plasma accelerators or laser guiding either through self-focusing or propagation of the laser through a plasma channel. In evaluating beat-waves as a possible method of electron acceleration, it is important to study any mechanisms which may damp the beat-wave or couple its energy into other plasma modes. Thus the next chapter addresses coupling between the beat-wave and the Raman backscatter instability.

Chapter 4

Coupling Between High-Frequency Plasma Waves in Laser-Plasma Interactions

4.1 Introduction

Waves in plasmas[31] is a major subtopic in the area of plasma physics. The nonlinear coupling between waves, although greatly investigated theoretically[39], remains relatively less explored in controlled laboratory experiments. An unmagnetized plasma can support two types of longitudinal waves: ion acoustic waves and electron plasma waves. If simultaneously excited in a plasma, the ion acoustic wave can couple a long wavelength plasma wave into shorter wavelength "quasi-modes" via quasi-resonant mode coupling[10]. The short wavelength quasi-modes can Landau damp thus dissipating energy of the original plasma wave. Such mode coupling has been seen in laser-plasma experiments[9]

and explained theoretically[10]. In this chapter we show instead, using experimental data and supporting simulations, the coupling between two electron plasma waves which have nearly the same frequency but very different wavenumbers. We find that the daughter waves generated in this mode coupling process take the energy preferentially from the short wavelength wave while the long wavelength wave acts essentially as a catalyst. Besides being of fundamental interest, this coupling could have implications for laser fusion (e.g.: coupling between Raman forward and backward plasma waves) and in plasma accelerators (e.g.: coupling between the small-k accelerating mode and Raman/Compton waves).

4.2 Theory

The dispersion relation of an electron plasma wave (w, k) in an unmagnetized plasma is given by $w^2 = w_p^2 + 3k^2 v_{th}^2$, where w_p is the plasma frequency and v_{th} is the thermal velocity of the plasma electrons. In the weakly damped limit, $(k\lambda_D)^2 \ll 1$ where λ_D is the Debye length, the thermal correction to the dispersion relation is small and $w \approx w_p$. Unlike coupling between ion acoustic and electron plasma waves[10], the mode coupling between two electron plasma waves generates modes at integer multiples of w_p. Therefore these modes are not, by themselves, natural modes of a plasma. To understand the coupling, we consider two electron plasma waves in a zero temperature plasma. Lagrangian coordinates are used because in these coordinates the two waves are separable. Relativistic corrections are higher order than the coupling effects and thus neglected in this derivation. The general position of an electron z is written as $z = z_0 + \xi$ where z_0 is the initial electron position and $\xi = \xi_1 + \xi_2$ is the perturbation due to the two plasma waves. The restoring force on the electrons is

$-eE$ where $E = 4\pi e n_0 (\xi_1 + \xi_2)$ from Gauss' law. The equation of motion is then $m\partial^2 z/\partial t^2 = -4\pi n_0 e^2 (\xi_1 + \xi_2)$, or $\partial^2(\xi_1 + \xi_2)/\partial t^2 = -w_p^2(\xi_1 + \xi_2)$. This is a simple harmonic oscillator equation with solutions that can be written as $\xi_{1,2} = \epsilon_{1,2} \sin(\psi_{1,2})/k_{1,2}$ where ϵ_1 and ϵ_2 are the amplitudes of the two waves in the Lagrangian frame, $\psi_{1,2} = (k_{1,2} z_0 - w_{1,2} t)$, and $w_1 \approx w_2 \approx w_p$. In the actual experiment w_1 and w_2 will not be exactly w_p because of thermal effects. The density perturbations can be calculated from the electron displacement using the equation:

$$\frac{\tilde{n}(z)}{n_o} = \left(\frac{\partial z}{\partial z_o}\right)^{-1} = \frac{1}{1 + \epsilon_1 \cos(\psi_1) + \epsilon_2 \cos(\psi_2)} \tag{4.1}$$

Lagrange's implicit function theorem can then be used to determine the density perturbations in the lab frame by eliminating z_0 (contained in $\psi_{1,2}$) in Eq. 4.1 resulting in the equation[19]

$$\frac{\tilde{n}(z)}{n_o} = \sum_{n=0}^{\infty} \frac{(-1)^n}{n!} \frac{\partial^n}{\partial z^n} [\xi_1(z,t) + \xi_2(z,t)]^n \tag{4.2}$$

The effect of an electron wave with a small wavenumber, k_2, on a large wavenumber, k_1, wave can be seen by expanding this equation to third order under the assumption $k_1 \gg k_2$ and $\tilde{n}(z)/n_0 \ll 1$:

$$\begin{aligned}
\frac{\tilde{n}}{n_0} &= 1 - \epsilon_1 \left(1 - \left(\frac{\epsilon_2 k_1}{2 k_2}\right)^2\right) \cos(\psi_1) - \epsilon_2 \cos(\psi_2) \\
&\quad - \epsilon_1 \left(\frac{\epsilon_2 k_1}{2 k_2}\right) (\cos(\psi_1 - \psi_2) - \cos(\psi_1 + \psi_2)) \\
&\quad - \frac{\epsilon_1}{2} \left(\frac{\epsilon_2 k_1}{2 k_2}\right)^2 (\cos(\psi_1 - 2\psi_2) + \cos(\psi_1 + 2\psi_2)) \tag{4.3}
\end{aligned}$$

The phase velocity of a wave of a given frequency is inversely proportional to its wavenumber, $v_{ph} = w/k$. Since in the experiment $v_{ph}(k_2) \approx c$ whereas $v_{ph}(k_1) \ll c$, the small wavenumber, k_2, wave will be referred to as the "fast wave" and the

k_1 wave as the "slow wave" throughout this Letter. Unlike the harmonics of a single wave which are small compared to the fundamental, the amplitude of the coupled waves in Eq. 4.3 can be as large or larger than the slow wave if the amplitude, ϵ_2, of the fast wave is on the order of the ratio of the wavenumbers ($\epsilon_2 \approx 2k_2/k_1$). This amplitude can be very small: for instance $2k_2/k_1 \approx 3\%$ for fast waves from forward Raman or from beat excitation coupling to a slow wave from backward Raman in an underdense plasma of density $n/n_{crit} \approx 10^{-3}$. As is evident in Eq. 4.3, the amplitude of the slow wave is reduced by this coupling while the fast wave is unaffected. Physically, this is because the displacement of the electrons by the fast wave can be on the order of the wavelength of the slow waves, but the displacement of the electrons by the slow wave is negligible compared to the wavelength of the fast wave.

4.3 Experiment

To experimentally demonstrate this electron plasma wave coupling, we excite two such plasmons with a wavenumber ratio $k_1/k_2 = 70$. This is done in the following manner: A short but intense laser pulse containing two frequencies (w_a, w_b) is fired into a plasma such that the frequency difference is $w_a - w_b \approx w_p$. This resonantly excites a plasma oscillation through the process of collinear optical mixing with a relativistic phase velocity (fast wave) at the resonant frequency $w_2 \approx w_p$ and wavenumber $k_2 = k_a - k_b$, the difference in the wavenumbers of the two laser modes[15]. Two slow-wave modes at (w_{1a}, k_{1a}) and (w_{1b}, k_{1b}) are also excited via a three wave parametric process, the stimulated Raman backscatter instability (SRS)[40], when the laser pulse exceeds the instability threshold. The wavenumbers of these modes are close to twice the wavenumbers of the two laser

modes, i.e. $k_{1_{a,b}} = 2k_{a,b} - w_p/c$. There is little coupling between the two slow waves as they have similar wavenumbers. However the fast wave, with a k of $1/70$ of the slow waves, strongly modifies the modal structure of the slow waves, generating daughter plasma modes at $(w_{1_{a,b}} \pm nw_2, k_{1_{a,b}} \pm nk_2)$.

In the experiment, where the fast and slow waves are driven by collinear optical mixing and SRS respectively, the amplitudes of the daughter modes will be modified by coupling to both the laser and the ions. Although stimulated Brillouin scattering (SBS)[40] grows more slowly than the SRS, the SRS backscatter of the higher frequency pump beats with the lower frequency pump, forcing the growth of a standing wave ion perturbation at wavenumber $2k_b$, twice the k of the lower frequency laser line. This can seed SBS[41] on that laser line. The SBS instability at $2k_b$ has approximately the same frequency and wavenumber as the slow/fast wave coupling at $w_{1_a} - w_2 \approx 0$, $k_{1_a} - k_2 \approx 2k_b$ and thus strongly perturbs this mode. This ion ripple can also affect the other plasma modes through electron/ion wave coupling. Complicating the matter further, the modes near zero frequency may be ion or electron Landau damped. Thus we expect to reproduce in the experiment the frequency and wavenumber spectra of the coupled modes only in a qualitative sense. The experimental set-up has been described in detail elsewhere[6]. Briefly, a CO_2 laser operating on two lines, 10.29 μm and 10.59 μm, first creates the plasma by tunneling ionization of static gas, 140 mTorr H_2, and then drives the fast and slow plasma waves as discussed above. The laser has a peak intensity of about 2×10^{14} W/cm^2 divided roughly equally between the two lines. The resonant plasma density is $\approx 9 \times 10^{15}$ cm^{-3}. The laser risetime is $\approx$ 100 psec and has a pulsewidth 300 psecs FWHM. Collective Thomson scattering of a probe laser is used to measure the plasma density fluctuations associated

with the slow wave and coupled waves. The incident angle of the 2ns (FWHM), 50MW, 0.53 μm optical probe laser beam is chosen to k-match to the k_{1_a} Raman backscatter mode. Although not perfectly k-matched, the coupled slow waves ($k_1 \pm nk_2$) also appear on the Thomson scattering diagnostic. To gain the maximum information about the modes, we resolve the frequency of scattered light in both time $w(t)$, using a spherically focused probe beam and a streak camera, and wavenumber $w(k)$, using a cylindrically focused probe beam[6, 24]. By resolving the evolution of the frequency spectrum versus time, we distinguish between the electron waves and the ion-wave-related features which occur later in time. The $w(k)$ resolved measurements on the other hand allow us to associate a wavenumber with each frequency and show the shift of (nw_2, nk_2) associated with coupling with the fast wave. The time resolved measurements have a time resolution of 20 psec and w resolution of 0.1 w_p, while the k resolved data has a resolution of 0.3 w_p/c in wavenumber and 0.3 w_p in frequency.

Figure 4.1(a) shows the time resolved spectrum around k_1 when a single wavelength (10.59 μm) laser beam is fired into the plasma. We clearly see a relatively narrow feature characteristic of strongly driven SRS[40] at w_p that lasts for 40 psec FWHM before evolving into a Compton spectra[12]. Figure 4.1(b) shows the time resolved spectrum around k_2 when a two frequency laser is fired into the resonant density plasma and excites the fast wave. The signal at w_p is the fast wave and that at $2w_p$ is the second harmonic of the fast wave at wavenumber $2k_p$. The ratio of the two signals and their absolute levels indicate a peak fast wave amplitude of $\approx$20%[6]. Figure 4.1(c) shows the time resolved frequency spectrum around k_1 (slow waves) when a dual frequency laser beam is fired into the plasma. In addition to the SRS modes from both lines appearing near w_p one now sees a

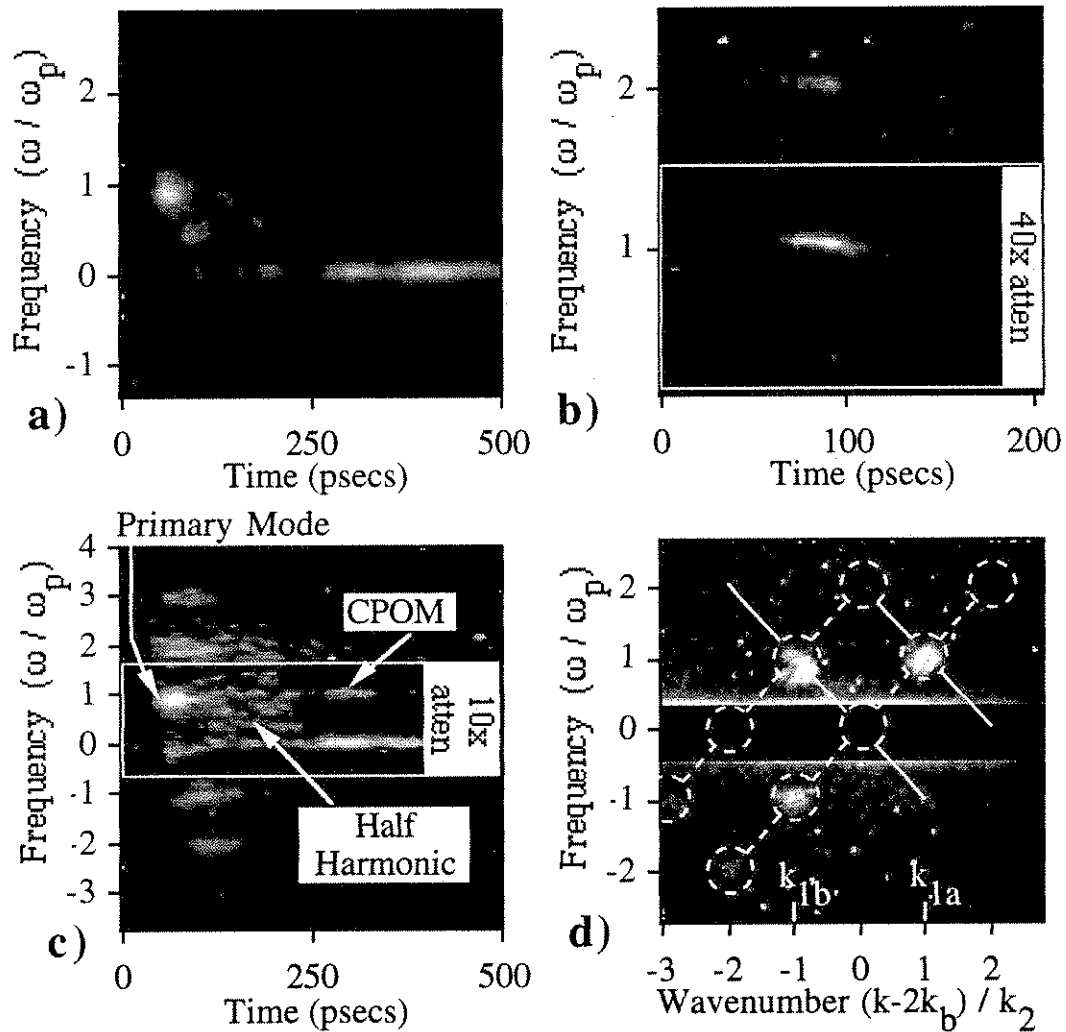Figure 4.1: Experimental results: (a) Time resolved slow wave (Raman) spectrum, single frequency laser; (b) time resolved fast wave spectrum, two frequency laser; (c) time resolved slow wave spectrum, two frequency laser; (d) coupled slow wave spectrum, (w, k) resolved, two frequency laser. Dotted lines connect circled Raman modes coupled by fast wave. Solid lines mark the expected spectrum of Compton scattering.

series of modes at $w_1 + nw_2$ where $-4 \leq n \leq 2$. The mode near zero frequency appears weak because of the 10x attenuator placed over the frequency range of -0.5 w_p to 1.5 w_p. It is slightly below zero frequency, which is marked by the long tail of SBS extending beyond 500 psec, indicating that the Raman backscatter frequency w_1 is slightly below the fast wave frequency w_2. This may be caused by Raman wave-breaking[12] or growth of Raman before full tunneling ionization of the plasma has been obtained. The coupled modes appear rather broad because the Raman is in the strongly driven regime[40]. The coupled modes typically last for 40 to 75 psec FWHM as evidenced by the broad feature at $w = 3w_p$, in good agreement with the lifetime of the k_1 mode at $w = w_p$ and that of the k_2 mode shown in Fig. 4.1(b). The peak of the coupled modes occurs later than the Raman mode at w_p because the fast wave amplitude is increasing, transferring more energy out to the coupled modes. There is a narrow well defined feature at w_p labeled as CPOM which extends out to 350 psec from the broad primary k_1 Raman mode. One possibility is counter propagating optical mixing (CPOM) which occurs when SBS of the pump laser waves produces counterpropagating 10.59 μm and 10.29 μm waves. The beating of the forward and backward propagating pumps produces a relatively narrow resonant response of the plasma at w_p[9]. Another explanation is electron/ion wave coupling which would also have a narrow well defined frequency and long time duration[9]. In addition to these we have often seen enhancement of scattering at about $\frac{1}{2}w_p$ which is as yet unexplained[42]. The feature at $\frac{1}{2}w_p$ can be seen in Fig. 4.1(c) about 50 psec after the peak of the fast/slow wave coupling.

That the coupled modes are indeed discrete in k space can be seen in the $w(k)$ spectrum of the slow waves shown in Fig. 4.1(d). Here, the two primary modes

due to Raman can be clearly seen near w_p and separated by $2k_2$ as expected. The Raman mode due to 10.59 μm in this particular example extends to frequencies somewhat below w_p. This is believed to be due to wavebreaking of the oscillation and its evolution into Compton scattering[12]. This downshifting is also evident in the time resolved spectrum of the single frequency Raman shown in Fig. 4.1(a). Coupled modes at near zero frequency shift are not seen because they are under a mask which blocks the stray light. The positions of the expected coupled modes are shown by circles on the dotted lines. The dotted lines have a slope $\partial w/\partial k = w_2/k_2 = c$ and the coupled modes lie on these lines separated by (w_2, k_2). The coupled modes of the 10.29 μm Raman (k_{1a}) at $n = +1$, -2 and -3 ($2w_p$, $-w_p$, and $-2w_p$) and that of the 10.59 μm (k_{1b}) Raman at $n = +1$ and -2 ($2w_p$ and $-w_p$) are clearly visible. Although not visible in this particular example, Compton spectra from the plasma after wave-breaking is often seen along the two solid white lines[12]. As the white line indicates, the 10.59 μm Compton scattering often extends below the mask on the blue side. This is because the Compton spectra from the 10.29 μm laser line, having frequency components less than w_2, couples with the fast wave, producing features with $w = w_{1a} - w_2 < 0$.

4.4   Simulations

These results were reproduced with the electromagnetic particle-in-cell (PIC) simulations using the code WAVE[27]. To show the theoretically predicted coupling between plasmons of widely differing k's without the complications of the two laser pulses, plasmons at wavenumbers k_1 and k_2 were excited at a frequency w_p using periodic longitudinal forces of the form $F = F_1 + F_2$ where

Figure 4.2: PIC simulations showing coupling of slow and fast electron plasma waves. Results from the $F_{1,2}$ driver are shown in Figs. (a)-(c). Spectrum of the density perturbation $(\tilde{n}/n_0)$ vs. time for modes near: (a) k_1; and (b) k_2. (c) Time histories of particular modes: (1) fast wave (k_2) whether or not slow wave (k_1) is driven. (2) slow wave if fast wave is not driven. (3) slow wave if fast wave is driven. (4), (5) coupled modes at $(2w_p, k_1 + k_2)$ and $(0w_p, k_1 - k_2)$, respectively. Curves (3)-(5) are taken from (b). (d) Time integrated (w, k) spectrum $(\tilde{n}/n_0)$ of the coupling between Raman waves and a beat-excited fast wave.
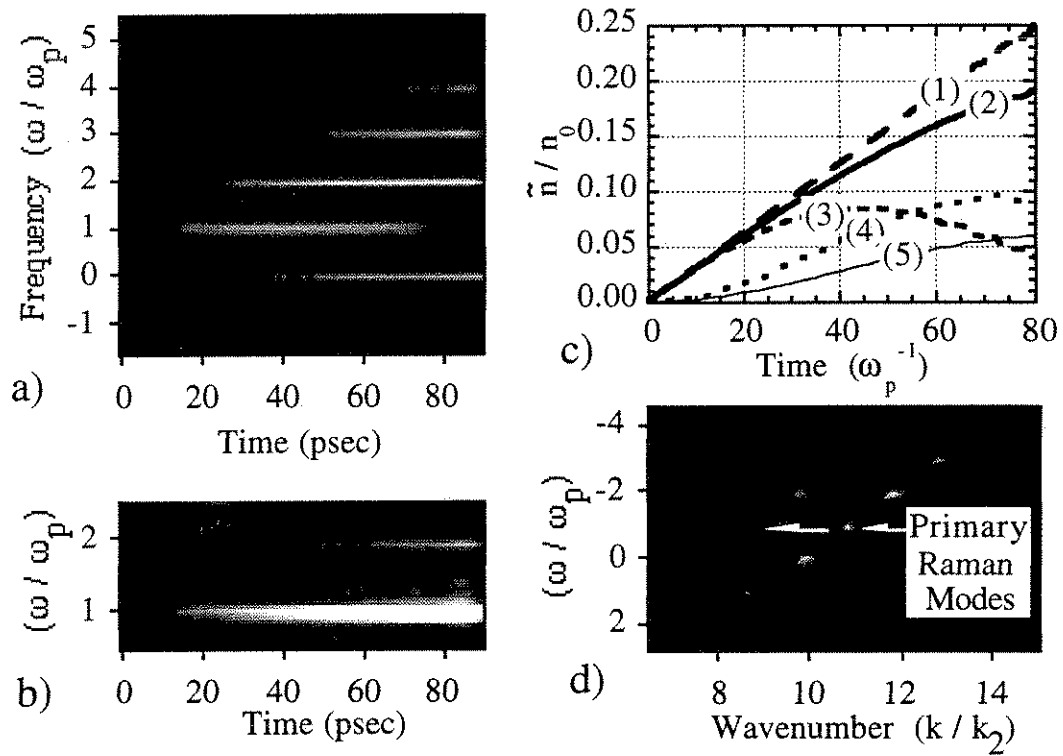
Figure 4.2: PIC simulations showing coupling of slow and fast electron plasma waves. Results from the $F_{1,2}$ driver are shown in Figs. (a)-(c). Spectrum of the density perturbation ($\tilde{n}/n_0$) vs. time for modes near: (a) k_1; and (b) k_2. (c) Time histories of particular modes: (1) fast wave (k_2) whether or not slow wave (k_1) is driven. (2) slow wave if fast wave is not driven. (3) slow wave if fast wave is driven. (4), (5) coupled modes at ($2w_p, k_1 + k_2$) and ($0w_p, k_1 - k_2$), respectively. Curves (3)-(5) are taken from (b). (d) Time integrated (w, k) spectrum ($\tilde{n}/n_0$) of the coupling between Raman waves and a beat-excited fast wave.
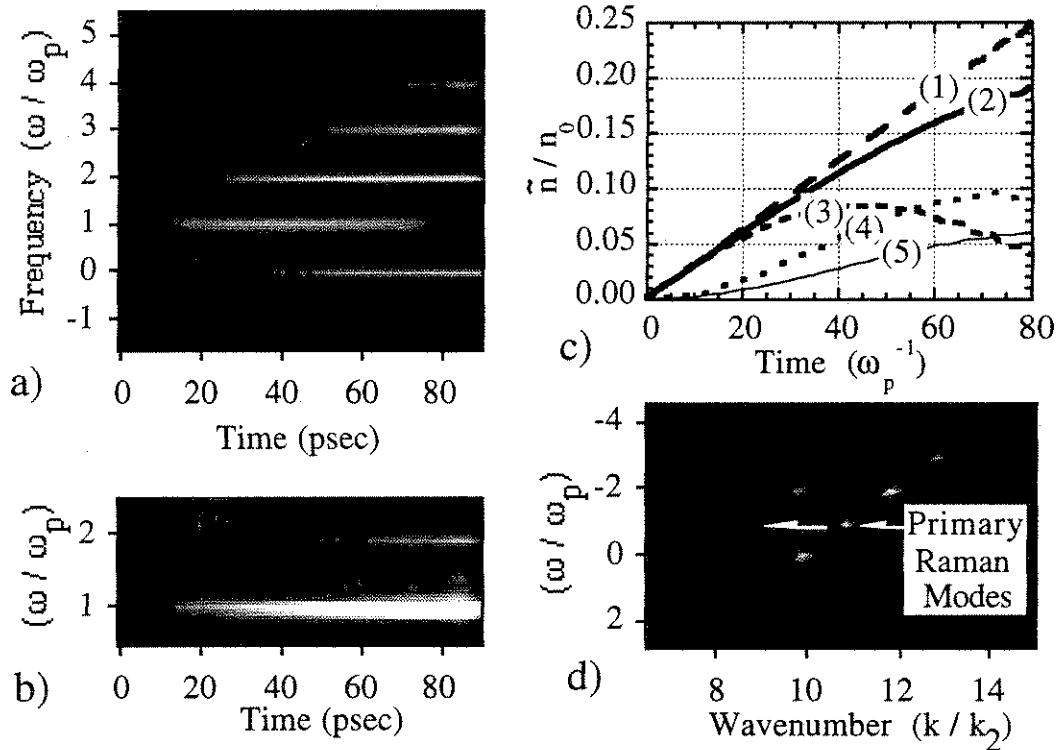
Chapter 5

Evolution of Stimulated Raman into Stimulated Compton Scattering of Laser Light via Wave-Breaking of Plasma Waves

5.1 Introduction

When an intense laser pulse interacts with an underdense plasma a number of parametric instabilities can be excited[43]. These instabilities have been under intense investigation for over a decade because of their role in laser fusion[44] and laser-driven collective plasma accelerators [14]. Experimentally, there is now ample evidence for these instabilities, yet their nonlinear evolution via wave-particle and wave-wave interactions remains poorly documented in experiments. In this letter we show, using experimental data and supporting simulations, how one

such instability, stimulated Raman backscattering (SRS)[45] evolves into stimulated Compton scattering (SCS)[46] via wave-breaking of Raman plasmons.

The SRS and SCS instabilities can be viewed as the low and high plasma temperature regimes of the same instability, consisting of: an incident laser (w_0, k_0), a backscattered light beam (w_b, k_b), and an electron plasma wave (w, k), where $w = w_0 - w_b$, $k = k_0 + k_b$. The dispersion relation which describes both instabilities is well known and given by[40]

$$1 + \chi_e = -\frac{\chi_e}{4} k^2 v_0^2 (w_b^2 - w_p^2 - c^2 k_b^2)^{-1} \tag{5.1}$$

$$\text{with } \chi_e = \frac{-w_p^2}{k^2} \int \frac{\partial \hat{f}_0 / \partial v}{v - w/k} \partial v \tag{5.2}$$

where the anti-Stokes term has been dropped. For a Maxwellian plasma the velocity distribution function, $\hat{f}_0$, is given by $\hat{f}_0 = exp(-v^2/2v_{th}^2)/(v_{th}\sqrt{2\pi})$ where $v_{th} = \sqrt{kT/m}$ is the electron thermal velocity.

SRS occurs when $k\lambda_D < 1/\sqrt{3}$ where $\lambda_D = v_{th}/w_p$ is the plasma Debye length. It is a coherent response of the entire plasma characterized by a relatively narrow frequency spectrum at $w^2 = w_p^2 + 3k^2 v_{th}^2$ with a dispersion relation $\partial w/\partial k = -c/2$ where c is the speed of light. The SCS instability $(k\lambda_D > 1/\sqrt{3})$ is primarily an interaction between "resonant" electrons (those electrons traveling near the phase velocity, w/k, of the plasma wave) and the light waves. It is characterized by a broad spectrum and a dispersion relation $\partial w/\partial k = -c$.

Previously, the saturation of SRS via wave-breaking has been seen in computer simulations[47]. In this letter, we document the self-consistent evolution of SRS into SCS by actually measuring the w and k spectrum of the plasma waves. We find that the spectrum is initially reasonably consistent with what is expected from strongly driven SRS but evolves into a broad SCS spectrum. We also observe

this in computer simulations which show that the broadening of the spectrum coincides with the wave-breaking of the plasma wave.

5.2 Experimental Setup

We begin with the experiment. A CO_2 laser first creates the plasma by tunnel ionization of static gas, 71 mTorr H_2, and then drives the instabilities in the plasma. The laser produces about 60 J of 10.6 μm light per pulse with a rise time of about 150 psec and a FWHM of about 300 psec. The linearly polarized laser is focused using an f/11.5 off-axis parabolic mirror to a spot diameter (1/e) of 300 μm which is about 4 c/w_p wide. The peak focal spot intensity thus approaches 6×10^{14} W/cm^2 or in normalized units $v_o/c = eE/mw_0c \approx 0.2$. Here E is the electric field of the laser. The gas is fully ionized within the first 20 psec by the laser over approximately ± 1 cm on either side of the best focus producing a plasma density of 4.7×10^{15} cm^{-3} or n/n_c of 4.7×10^{-4}. Based on tunnel ionization theory[16], the initial plasma temperature at ionization is about 75 eV in the direction of polarization of the laser and less than 1 eV in the other two directions[48]. The actual longitudinal temperature based on the experimental results is 6-10 eV, indicating some transfer of energy from the transverse direction. Ion effects play a minimal role because the laser pulse is only five ion periods long.

We use collective Thomson scattering to measure the plasma density fluctuations associated with SRS and SCS[24]. The incident angle of the 2ns (FWHM), 50MW, 0.53 μm optical probe beam is chosen such that the incident (w_{pr}, k_{pr}) and the scattered light (w_s, k_s) will k-match to the Raman/Compton waves. To gain the maximum information about the SRS/SCS density fluctuations in the plasma, we resolve the frequency of scattered light in both time $w(t)$ and wavenumber

$w(k)$. By resolving the evolution of the frequency spectrum versus time $w(t)$, we observe signatures of the growth and breaking of Raman plasmons and their evolution into Compton. The $w(k)$ resolved measurements on the other hand allow us to associate a wavenumber with each frequency in the time resolved data and show for the first time the dispersion relation for the SCS fluctuations.

Thomson scattering of a probe laser from the plasma measures both w and k of the density perturbations as a function of time because the scattered light is shifted by the w and k of the plasma wave. However, as the data must be collected on a camera which has only 2 dimensions, the frequency spectrum can only be measured as a function of time or wavenumber, not both in a single laser shot.
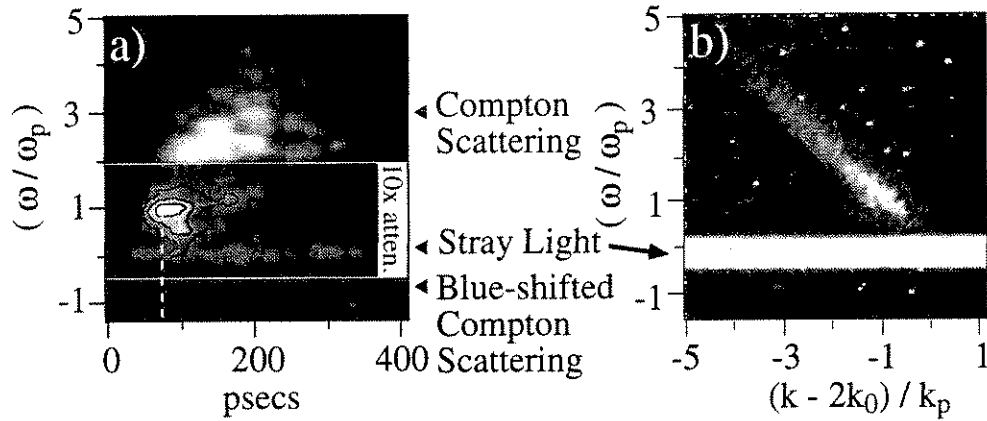

Figure 5.1: Log plots of single shot SRS/SCS spectra measured by a Thomson scattered probe beam. (a) Time resolved spectrum showing evolution of SRS into SCS through wave-breaking. Central region bounded by the two solid white lines is 10 times attenuated. Contour lines are at $\frac{3}{4}$, $\frac{3}{8}$, and $\frac{3}{16}$ of peak scattering intensity. Dotted line indicates time at which Raman amplitude was measured. (b) Wavenumber and frequency resolved signal showing the broad Compton scattering spectrum with the characteristic SCS dispersion relation $\partial w/\partial k = -c$. Here $k_p = w_p/c$.

For $w(t)$ resolved measurements of the plasma waves, it is necessary to collect a range of scattering angles and re-image them to a small spot which can then

be dispersed in w and t. This is accomplished by using a probe beam which is spherically focused by an $f/30$ lens to a 200μm diameter in the center of the plasma. A lens at the correct k scattering angle then collects the k spectrum of interest and images it onto the input slit of an imaging spectrometer. The output spectrum from the spectrometer is dispersed in time on the other axis by a streak camera with a 20 psec resolution producing the $w(t)$ spectrum shown in Fig. 5.1(a). This set-up cannot be used for fine k-resolved measurements because its k resolution is limited by the cone angle of the probe beam to $2\pi/(\lambda_{pr}f^{\#}) = 0.4$ μm^{-1} while the required k resolution is better than $w_p/c = 1.5 \times 10^{-2}$ μm^{-1}.

To obtain $w(k)$ resolved spectra with adequate k resolution for a single shot determination of the dispersion relation, we use a cylindrically focused probe laser. The 6 mm long line focus minimizes the perpendicular k spread of the laser on one axis, allowing high k resolution in that direction (Fig. 5.1(b)). For this case, the quality of the probe beam and optics limit the k resolution to about 5×10^{-3} μm^{-1}, 80 times better resolution than the conventional experimental set-up using a spherical lens and 3 times finer than w_p/c. These are the most detailed $w(k)$ spectra obtained in any laser-plasma experiment to date.

5.3 Results

The basic features of the time and wavenumber resolved spectra shown in Fig. 5.1 (a) and (b) are as follows: The spectrum is time resolved with a frequency resolution of 0.2 w_p in Fig. 5.1(a). It begins with a relatively intense burst of Raman shown by the inner contour line that peaks at approximately the w_p corresponding to fully ionized density. This implies that the plasma is relatively cold

and the thermal correction to the Bohm-Gross frequency is small. The deconvolved bandwidth of the Raman, measured as $\approx 0.25 w_p$ (FWHM), is dominated by strong coupling of the intense laser. Its width corresponds to 8 e-foldings of the spectral growth curve given by the numerical solution to Eq. (1) with a laser v_0/c fixed at 0.1. A scan taken through this data at time $t = 70$ psec gives a maximum density fluctuation level $\hat{n}/n_0$=8%-15% using the usual Bragg scattering formula[26]. Assuming that this level is determined by wave-breaking[49] (to be justified later) we can infer a $k\lambda_D$ for the Raman wave of 0.31 to 0.4 and thus a plasma temperature of between 6-10eV.

The intense portion of this burst splits into two components, one shown by the second contour that rapidly decreases in frequency and the other, seen most clearly in the third contour, that remains near w_p. We will show by comparison to PIC simulations later that the component which shows a sudden decrease in frequency is characteristic of wave-breaking of the two-dimensional Raman oscillation on axis (where it presumably has the largest amplitude). Coincident with this, the Thomson scattering shows the development of a weaker but much broader spectrum which eventually extends to 0.7 w_p on the blue side and 4.5 w_p on the red side of zero frequency. We believe this spectrum is a result of Compton scattering in the non-Maxwellian plasma.

The wavenumber resolved frequency spectrum, shown in Fig. 5.1(b), is dominated by the Compton scattering because it is a time integrated spectrum and Compton lasts much longer than the initial Raman burst. The most striking feature of this spectrum is that the slope is $\partial w/\partial k = -c$ showing that it is indeed Compton.
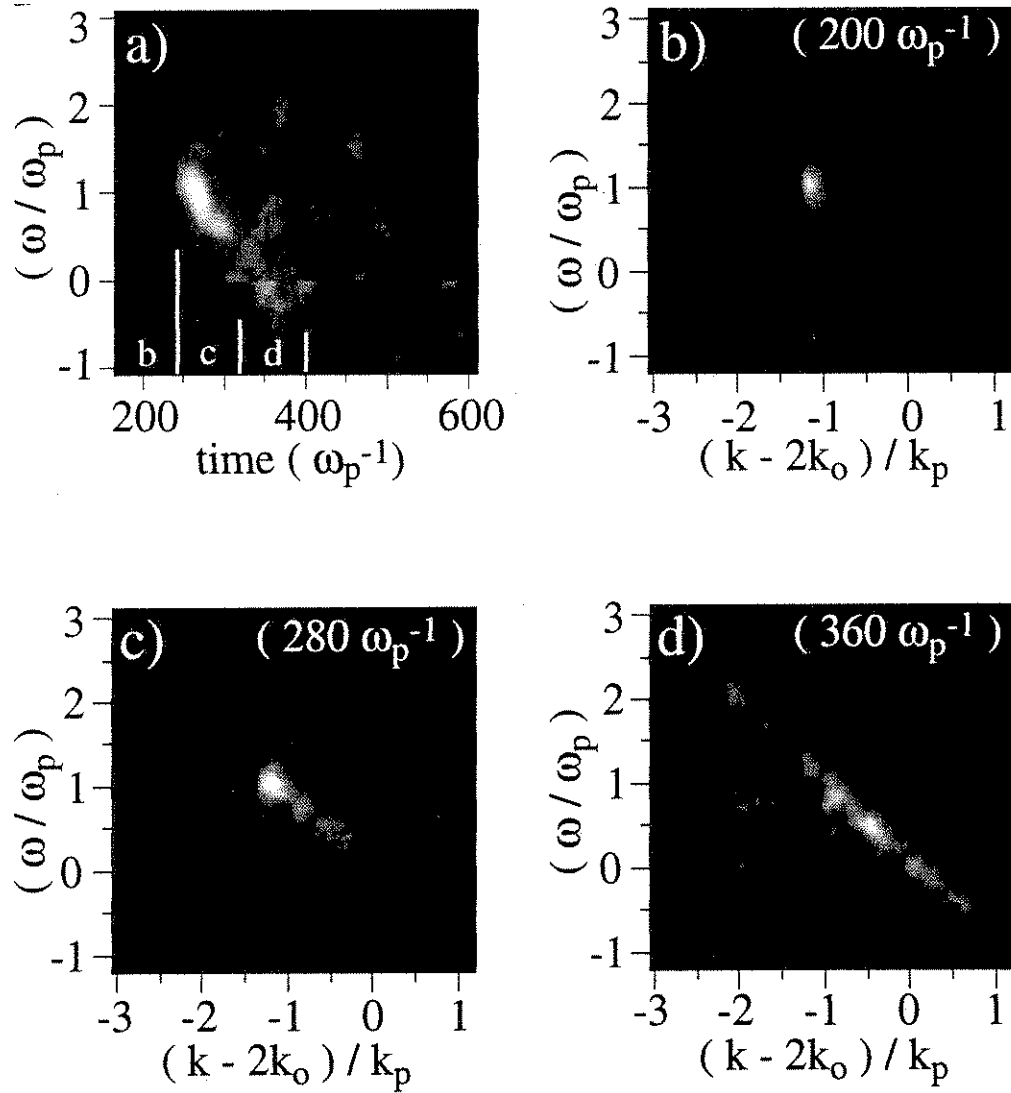
Figure 5.2: Simulation results showing evolution of SRS into SCS through wave-breaking. a) Time resolved frequency spectrum of plasma density fluctuations near $2k_0$ associated with SRS and SCS. Snapshots taken over intervals marked in plot a) showing $w(k)$ spectrum of: b) Raman instability, c) wave-breaking, d) Compton spectrum with blue-shifted components. Spectra b), c), and d) are all on the same scale, also showing the increase of background noise around $2k_0$ caused by wave-breaking.

a) b)
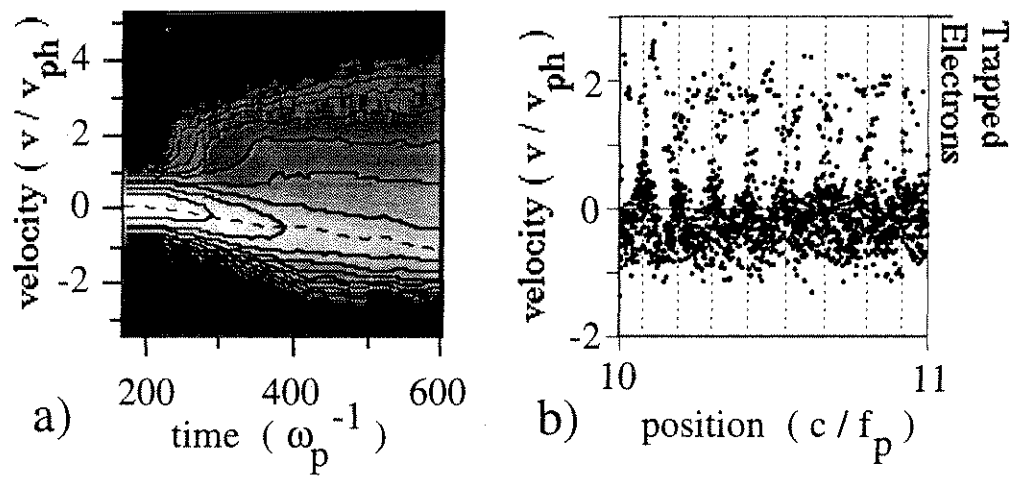
Figure 5.3: Velocity phase space plots for simulation. Velocity axis is normalized to $v_{ph} = w_p/(2k_0 - k_p)$, the initial phase velocity of the Raman wave. a) Evolution of velocity distribution function (log plot, 5 contours per factor of 10) from a relatively cold Maxwellian to a much hotter non-Maxwellian consisting of trapped electrons moving forward with phase velocities up to 4 v_{ph} and the main body of the electrons moving backward. The dotted line tracks the peak of the distribution function. b) Scatterplot of electron velocity vs. position showing periodicity of electron trapping at the wavenumber of the Raman, taken at 280 w_p^{-1}.

5.4 Simulations

In order to understand the details of the evolution of the Raman fluctuations into Compton fluctuations, we have used the particle-in-cell (PIC) code WAVE[27] because the plasma is neither Maxwellian nor linear during the evolution of SRS into SCS. In order to model the key features of the experiment, we use $k\lambda_D$ as the key parameter in PIC simulations. In the simulations we use $k\lambda_D = 0.38$ (corresponding to the plasma temperature in the experiment of 9eV), $w_0/w_p = 5$ and $v_0/c \approx 0.2$ and a pulse which rises in 300 w_p^{-1} then remains constant. The simulation box is 100 c/w_p long along the direction of propagation of the laser. Taking a Gabor transform[50] of the density at one point in the plasma provides the amplitude of each frequency component of the SRS/SCS density perturbations as a function of time (Fig. 5.2a), just like the spectrometer/streak camera combination does in the experiment. The discontinuity at zero frequency is a subtlety of the Gabor transform which has no effect on the overall spectrum. Also, to better visualize the evolution of SRS into SCS it is instructive to look at the temporal evolution of the $w(k)$ spectrum of plasma waves. This is done by breaking the time history of the plasma waves into sections that are each 80 w_p^{-1} long and then Fourier transforming them in time and space to produce the snapshots of the $w(k)$ spectrum of the plasma waves. Three snapshots taken at: 200 w_p^{-1} when the predominant mode is SRS; at 280 w_p^{-1} when SRS is wave-breaking and evolving into SCS, and at 360 w_p^{-1} when SCS is fully developed are shown in Fig. 5.2(b), (c) and (d). The interpretation of the $w(t)$ and $w(k)$ plots of Fig. 5.2 is aided by the phase space (v_x/v_{ph} vs. space) and (v_x/v_{ph} vs. time) plots, where v_{ph} is the theoretical phase velocity of the plasmons before wave-breaking and x is the direction of propagation of the laser beam. One such

example is shown in Fig. 5.3 (a) and (b) taken at 280 w_p^{-1} when wave-breaking occurs.

As in the experiment [Fig 5.1(a)], one sees SRS growing rapidly at $w = w_p$ and $k = 2k_0 - w_p/c$ in the simulations (Fig. 5.2 (a) and (b)). Its bandwidth is narrower than in the experiments because the coupling term from Eq. (1), $v_0 k$, is 5 times lower, reducing the strong coupling effects. The SRS begins to trap electrons once it grows to an amplitude of about 10%, in good agreement with the warm plasma wave-breaking theory[49]. These density perturbations continue to grow somewhat until the waves break. The onset of wave-breaking occurs at 280 w_p^{-1}. It is characterized by first, roughly 20% of the electrons being accelerated in the forward direction by the plasma wave and second, by the bulk of the plasma moving backwards generating a return current. This is clearly visible in Fig. 5.3 (a) and (b). At wave-breaking, some electrons are seen to gain velocities up to 3 v_{ph} while the bulk of the plasma at this time is moving backwards at $v_b = 0.3$ v_{ph}. Note that at this time there is still an oscillation at w_p [Fig. 5.2(c)], however its k spectrum is rapidly evolving from a well defined Bohm-Gross peak at $(2k_0 - w_p/c)$ into a much broader spectrum. The accelerated electrons are still very much bunched at the Raman wavenumber [Fig. 5.3(b)]. Consequently SCS does not have to grow from noise. The electron distribution function [Fig. 5.3(a)] at this time is far from Maxwellian. In fact it more closely resembles a bi-Maxwellian with a colder Maxwellian containing 80% of the particles drifting backwards in the lab frame and a second hotter Maxwellian containing 20% of the electrons drifting forward. Eventually some electrons are accelerated up to 4 times the phase velocity of the SRS plasmons. The return current that results from wave-breaking alters the $w(t)$ evolution. As shown in Fig. 5.2(a), the bright

SRS peak rapidly decreases in frequency, similar to one of the observed features in the experiment. This occurs because the primary response of the plasma is given by the cold electrons. As these electrons are moving towards the laser, in the opposite direction of the plasma wave, the plasma frequency is Doppler shifted in the lab frame by a factor $1 - v_b/v_{ph}$. In addition, the effective plasma density is reduced as the response of the hot electrons at the cold Raman frequency is small. This second effect is less important than the Doppler shift. Immediately after wave-breaking, the plasma spectrum rapidly broadens, a characteristic of SCS. The relationship between w and k for this spectrum shown in Fig. 5.2 (c) and (d) confirms that wave has indeed evolved into Compton after being heated by the Raman wave-breaking.

5.5 Discussion

An important difference between the simulations and the experiment is that the simulations are 1D whereas the experiment is 3D. Since the laser beam in the experiment has a transverse intensity profile that falls off as one moves away from the center, we expect the SRS wave to grow and break close to the center. This wave-breaking causes the return current to flow in the center region roughly c/w_p wide. It is in this region where the SRS frequency drops for the reasons described above. Away from the beam center, the plasma wave takes longer to break, thus producing the continuing enhancement of the spectrum near w_p in the experiment.

The crucial experimental confirmation that SRS evolution into SCS occurs via wave-breaking, which accelerates electrons and thus drives a return current, is the appearance of blue-shifted components of the Compton scattering seen both

in the experiment and in the simulations (Fig. 5.1(a) and Fig. 5.2(a)). These correspond to density fluctuations that are actually moving back toward the laser in the lab frame. The theoretical growth rate is zero for these fluctuations for a Maxwellian plasma. However, numerical solutions to Eq. (1) for non-Maxwellian plasmas show that growth of the blue-shifted Compton scattering occurs when a region on the negative velocity side of the electron distribution function has a negative slope ($\partial \hat{f}_0/\partial v < 0$ with $v < 0$). Such is the case when the return current in effect produces a backward drifting distribution function.

The evolution of SCS, $w(t)$ and $w(k)$, is qualitatively similar in both the experiment and simulations. At 360 w_p^{-1}, the $w(k)$ snapshot [Fig. 5.2(d)] shows the dispersion relationship of the SCS waves with the negative speed of light slope as does the experiment [Fig. 5.1(b)]. The simulations which are a snapshot in time again show the blue shifted frequency components which are not discernible in the time integrated $w(k)$ plot of Fig. 5.1(b). In a thermal plasma the SCS always has a maximum growth rate at $w > w_p$. However both the $w(t)$ and $w(k)$ space (Fig. 5.1 (a) and (b)) show Compton peaking close to 0.7 w_p. If the main body of the electrons constituting the return current were to move backwards at v_{ph} then the peak of the SRS/SCS fluctuations would be close to zero frequency. The peak in the experiment near 0.7 w_p indicates that the main body of the electrons is traveling backwards at less than the initial Raman phase velocity, a conclusion supported by the phase space plots of Fig. 5.3 and $w(k)$ plots of Fig. 5.2(d).

5.6 Conclusion

We have documented the evolution of the stimulated Compton scattering instability in an initially cold plasma. Stimulated Raman scattering occurs first. The SRS plasmons trap background plasma electrons which are both bunched at the correct k for SCS and accelerated over a broad velocity range up to $4 \, \mathrm{v}_{ph}$. At the same time the bulk of the plasma electrons drift backward to maintain charge neutrality. The SCS spectrum is then determined by this resulting nonthermal electron distribution.

Chapter 6

Conclusion

In this thesis some of the ongoing experiments, theory, and simulations aimed at further developing an understanding of, and improving, electron acceleration via plasma beat-waves have been documented. In Chapter 2, the time evolution of the amplitude and frequency of the beat-wave and its second harmonic were measured using direct Thomson scattering, showing that the peak beat-wave amplitude was between 22% and 44% with a duration of 100 psec (FWHM). The amplitude of the 2nd harmonic of the beat-wave relative to the fundamental was also in good agreement with the relationship between the beat-wave harmonics and fundamental given by $\delta n_l = A_l n_1^l$ where $A_1 = 1$, $A_2 = 1$, and $A_3 = 63/64$ derived analytically and confirmed through simulations to be ≈ 1. The limiting factor in beat-wave amplitude was shown through simulations to be expulsion of the plasma by the ponderomotive force of the laser and beat-wave. This plasma expulsion was also indicated in the experiment by the decrease in frequency of the beat-wave over time and the reduction in scattering by plasma electric and magnetic fields of a relativistic electron beam co-propagating with the CO_2 laser.

The first trapped particle acceleration of externally injected electrons by a plasma wave was presented in Chapter 3[8]. In this chapter, acceleration of a relativistic 2 MeV electron beam up to an energy of 30 MeV was presented, well above the kinetic energy of an electron moving synchronously with the wave, $0.511(\gamma_{ph} - 1) = 16$ MeV, where $\gamma_{ph} = (1 - v_{ph}^2/c^2)^{-1/2}$ is the Lorentz factor for the plasma wave and v_{ph} is the phase velocity. Trapping is important as it allows electrons to gain the theoretically maximum amount of energy limited by dephasing and can also bunch electrons in space and energy leading to a more useful accelerated electron beam.

In Chapter 4, electron-electron wave coupling between the beat-wave and the stimulated Raman backscatter instability (SRS-B) was presented using time and wavenumber resolved spectra of Thomson scattered light from the plasma. The qualitative features of the measured $w(t, k)$ spectra were predicted by a Lagrangian fluid description and reproduced in particle simulations. Electron-ion wave coupling between the beat-wave and ion waves generated by stimulated Brillouin scattering (SBS) had been seen before in laser-plasma experiments[9] and explained theoretically[10], but coupling between two electron waves with similar frequencies but greatly differing wavenumbers had not been considered before. Unlike the electron-ion wave coupling case where energy from the beat-wave was coupled into other modes, the daughter waves generated in the electron-electron wave coupling process took the energy preferentially from the SRS-B without significantly affecting the beat-wave. This result is important because in future beat-wave acceleration experiments the plasma wave will be driven on time scales shorter than an ion period, and thus electron-electron wave coupling will dominate over electron-ion wave coupling.

The stimulated Raman backscatter instability was studied further in Chapter 5. Evidence of wave-breaking of the Raman backscatter instability caused by trapping of background electrons was presented in the form of a sudden downshift in the Raman spectrum as it evolved into Compton scattering. This downshift of the spectrum was time resolved in the experiment via Thomson scattering and in 1D particle-in-cell (PIC) WAVE simulations via a Gabor transform of the plasma density perturbations. The downshift in frequency was caused by a return current in the form of the untrapped background electrons travelling towards the laser to compensate for the trapped electrons and maintain charge neutrality. This return current Doppler shifted the Raman backscatter light, causing a Raman frequency downshift in both the experiments and simulations.

A number of experiments are planned for the near future which will continue the progress in the development of the beat-wave accelerator concept. In terms of further diagnosing the actual beat-wave, the next step will be spatially resolved beat-wave measurements based on Thomson scattering. This can be accomplished by transforming the k spectrum of the Thomson scattered probe light into space with a cylindrical lens placed between the last spherical lens and the spectrometer slit in the Thomson scattering setup shown in Fig. 2.2 (a). With this setup, a time integrated spatial profile of the beat-wave and quite possibly its second harmonic can be obtained by operating the streak camera on a slow sweep speed, just like the w-k spectrum of Fig. 2.2 (c). This setup will not be able to temporally resolve the spatial profile of the beat-wave as both time and space will be on the same axis. If this measurement is successful, the streak camera will be rotated 90 degrees to change the time axis and thus measure the beat-wave amplitude in both space and time at the expense of the frequency resolution.

A number of experiments are also planned for measuring the effects of the beat-wave on the plasma and the evolution of the plasma after the beat-wave breaks up. The electron temperature of the plasma after excitation by a large amplitude beat-wave has already been measured at about 3 keV based on the spectrum of x-rays emitted by bremsstrahlung. This measurement agreed well with the plasma temperature after break up of the beat-wave in WAVE simulations which was also 3 keV. By imaging these x-rays through a pinhole onto a CCD camera an image of the hot region of the plasma will be obtained, providing an additional estimate of the spatial length of the beat-wave.

The electron beam will also be used to measure the electric and magnetic fields in the plasma during and after the excitation of the beat-wave, extending the electron scattering measurements of Chapter 2. By replacing the glass Cherenkov slide with an array of optical fibers, a quantitative measure of the scattering angle of the electron beam as a function of time can be obtained with 40 psec resolution, providing direct measurements of the strength of the transverse electric and magnetic fields in the plasma. By scanning the transverse position of the electron beam on a shot to shot basis, the transverse spatial profile of these fields in the plasma will be obtained. This diagnostic should allow detailed studies of both the break up of the magnetic fields associated with the beat-wave and the growth of the Weibel instability.

Looking further ahead, the group plans to build an intense short pulse (10 Terawatt peak power, 3 psec FWHM) 1 μm laser to generate beat-waves over lengths greater than 10 cm which should be able to accelerate electrons up to 1 GeV. Ponderomotive expulsion of the plasma, a serious issue for CO_2 lasers, will be avoided because of the length of the laser pulse. Thus, although a great deal

has been accomplished in the last few years, there is still much planned for the future.

Appendix A

Experimental Measured Parameters of CO_2 Laser

A.1 Generation and Measurement of Short (sub 500 psec) CO_2 Laser Pulses

A.1.1 Introduction

To drive a large amplitude beat-wave, while avoiding such undesirable effects such as ponderomotive blowout of the plasma by the laser and the growth of ion instabilities which can couple energy out of the beat-wave, a short laser pulse (below 500 psec) is required. Producing such a short pulse with a CO_2 oscillator is extremely difficult because of the narrow bandwidth of the CO_2 gas. However, once such a pulse is generated, high pressure ($\geq$ 1 Atm) CO_2 amplifiers can be used to amplify it while maintaining the pulse width below 500 psec. In addition to producing such pulses, measuring their temporal profile is important to confirm their short pulse length and determine the parameters for plasma

physics experiments. The lack of fast detectors at 10.6 μm makes it necessary to use non-linear optics to temporally resolve the pulses. In this appendix, we describe the generation of short (300 psec FWHM) intense (200 GW) pulses by a currently operating CO_2 laser (the Mars laser) at UCLA and their temporal measurement via the optical Kerr effect.

We begin with a description of the laser system and free induction decay which generates the short pulse, then explain how the optical Kerr effect converts the pulse to a signal at 0.53 μm which can be time resolved on a streak camera. Finally, we compare the pulse length measurements to a theoretical estimate of pulse length.

A.1.2   Details of CO_2 Laser System

The most unique part of this system is the conversion of a long 150 nsec CO_2 pulse into a short 60 psec pulse via optical free induction decay This is accomplished using a spark gap and a hot CO_2 absorber. The long pulse from the oscillator is focused through a spark gap which is triggered at the peak of the laser pulse. When the spark gap fires, it produces a plasma in the focal spot of the pulse which rapidly propagates throughout the focal region via electron cascading in the strong electric fields of the laser. This plasma reflects the back half of the laser pulse, chopping the pulse at its peak in about 50 psec. The chopped pulse is triple passed through a 3 meter tube containing 40 mTorr of CO_2 gas at 350° C, a temperature at which there are a large number of electrons in the lower level of the lasing line. Because the bandwidth of the absorbing cell is larger than than the initial bandwidth of the pulse, all the laser radiation is absorbed. However, when the pulse abruptly shuts off, the atoms in the absorber cell continue to oscillate in

phase for a short time, generating a pulse of radiation approximately 60 psec long at the frequency of the input pulse. This is known as optical free induction decay. Another way of looking at it is that the absorber cell has a narrow bandwidth and is thus unable to absorb the additional frequencies generated by chopping the pulse. The pulse emitted from the absorber cell then consists of the unabsorbed radiation.
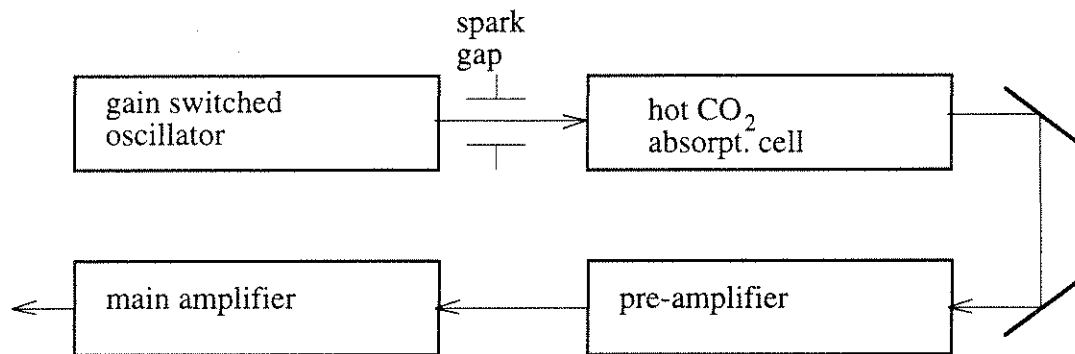
Figure A.1: Schematic of Mars Laser

The oscillator used to produce the pulse for the optical free induction decay is rather specialized. The pulse it produces must have the narrow bandwidth of a low pressure laser (LPL) to insure that its energy will be completely absorbed by the absorber cell, but have the power output of a 1 Atm CO_2 laser to continue the formation of plasma initiated by the spark gap. In addition, as many of the experiments in the lab involve two-frequency excitation of plasmas, the oscillator must be capable of two-frequency operation. To accomplish all of these things, we use a hybrid gain-switched CO_2 oscillator containing a low pressure (22 mTorr) gain cell, a 1 Atmosphere gain cell and an absorbing cell within the cavity (figure A.2).

The low pressure cell (LPL) fires first, seeding the cavity with single longitudinal mode radiation on the various gain lines of the CO_2 gas. Single mode radiation is produced because the gain bandwidth of each transition in the LPL is 2.3×10^8 s^{-1}, narrower than the 6×10^8 s^{-1} spacing between longitudinal modes in the cavity. After the LPL fires, the main 1 Atm gain cell fires, amplifying the seed pulses up to 1 Joule in a 150 nsec pulse. These high energy pulses remain single mode since the seed radiation dominates over the background noise spectrum.

Most CO_2 laser operate at 10.6 μm because the gain of this wavelength dominates over other wavelengths. To reduce the gain near 10.6 μm, an absorption cell is used. By controlling the partial pressures in the cell of various gases which absorb regions of the CO_2 gain spectrum, the oscillator can be operated in either single frequency mode or in any combination of the 9.6, 10.3, and 10.6 μm laser lines. To fine tune the gain in each laser line, we adjust the cavity length using the rear reflector which is mounted on a piezo-electric.

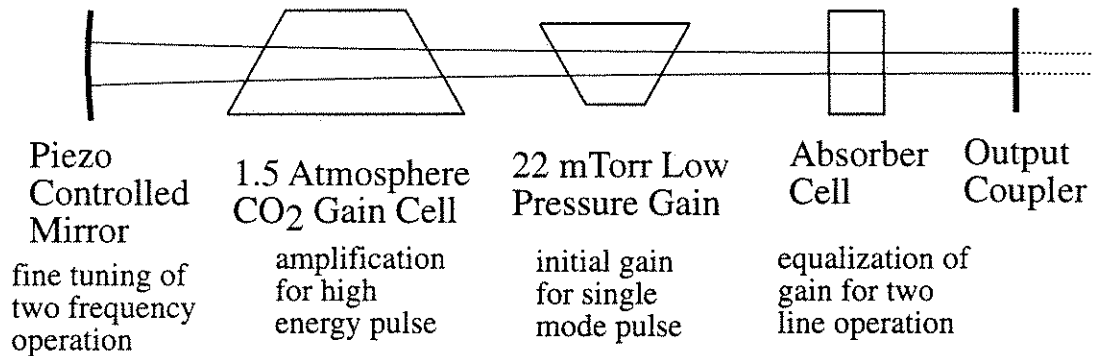| Piezo Controlled Mirror	1.5 Atmosphere CO_2 Gain Cell	22 mTorr Low Pressure Gain	Absorber Cell	Output Coupler
fine tuning of two frequency operation	amplification for high energy pulse	initial gain for single mode pulse	equalization of gain for two line operation	

Figure A.2: Diagram of Hybrid Oscillator

After the pulse is converted to a short pulse via optical free induction decay, it

is amplified by a factor of 10 in a 1 Atm TEA pre-amplifier, and by a factor of 10^5 in the main 2.3 Atm amplifier (figure A.1) to a total energy of up to 150 Joules. Because of the limited bandwidth of these amplifiers, the pulse is broadened by gain narrowing according to the formula[51]

$$\tau_p^2(z) = \tau_p^2(0) + \tau_g^2 \quad \text{where } \tau_g^2 = \frac{16 \ln 2 \ln G_0}{\Delta w_a^2} \tag{A.1}$$

In this equation $\tau_p(0)$ is the original pulse length, G_0 is the gain and Δw_a is the gain bandwidth. The gain bandwidth of CO_2 amplifiers with pressures greater than 5 torr is dominated by pressure broadening. Thus the pre-amplifier, which operates at only 1 Atmosphere causes the majority of the gain narrowing and pulse broadening even though most of the amplification is done in the main amplifier. For the pre-amplifier, G_0 is 10 and $\Delta w_a/(2\pi)$ is 3.7 GHz, giving a τ_{g1} of 215 psec, while for the amplifier, which runs at 2.3Atm, τ_{g2} is 156 psec. Thus the 60 psec input pulse should broaden to $\tau_p = (\tau_p^2(0) + \tau_{g1}^2 + \tau_{g2}^2)^{1/2} = 274$ psec.

A.1.3 Pulse Measurement via Optical Kerr Effect

Although we can estimate the pulse length at just under 300 psec based on theoretical considerations, standard measurement techniques for 10.6μm light are limited to approximately 500 psec resolution for cold detectors and a nanosecond for photon drag detectors, making it difficult to confirm the pulse length or measure the temporal profile. To resolve this pulse in the picosecond regime it is necessary to use a streak camera, which can only detect visible or near-visible light. Thus, to time resolve the CO_2 laser pulse, we must use the CO_2 pulse to affect visible light, and then time resolve the effect on the visible light. We use the Optical (AC) Kerr Effect to modify the polarization of a green probe beam with the CO_2 light and measure this effect on a Hamamatsu C979 streak camera.

The resolution of this experiment was limited only by the 30 psec resolution of the streak camera as the response time of the carbon disulfide Kerr medium is two picoseconds[52].

The Optical Kerr Effect is bi-refringence in a medium caused by interaction of an intense polarized optical beam with the medium which increases the index of refraction in the direction of the electric field (the direction of polarization) relative to the magnetic field direction by n_2I, where n_2 is the Kerr coefficient of the medium. This bi-refringence can be used to affect a doubled yag (532 nm) probed beam which can then be streaked on a streak camera, providing information about the CO_2 laser pulse intensity with 30 psec temporal resolution . If the CO_2 and probe lasers co-propagate in a Kerr medium with polarizations separated by an angle θ, the Kerr effect will modify the polarization of the probe laser, converting it from linear polarization in the $\hat{x}$ direction to elliptical polarization with a component in the $\hat{y}$ direction. This change in polarization can be converted into a variation in intensity by using crossed polarizers and then streaked, measuring the intensity of the CO_2 pulse as a function of time.
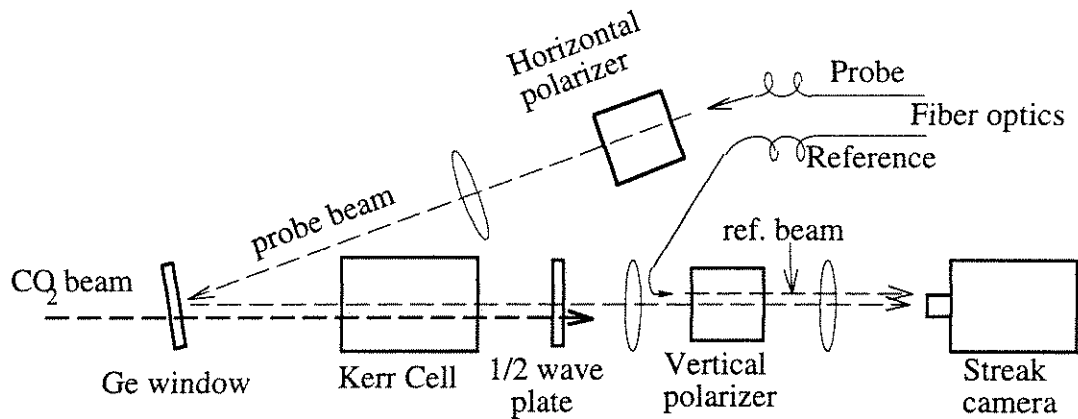

Figure A.3: Schematic of Kerr Cell Experiment

As shown in figure A.3, light from a 5 nsec FWHM, 532nm doubled Spectra Physics DCR11 Q-switched yag laser pulse is brought to the experiment by a multi-mode fiber and then polarized in the $(\hat{x})$ direction by a horizontal polarizer. The light is then sampled by a vertical $(\hat{y})$ polarizer after co-propagating with the CO_2 pulse through a Kerr cell containing carbon disulfide. Because the polarizers are crossed, light will only reach the streak camera when the CO_2 laser light modifies the probe polarization in the Kerr cell through the Kerr effect. The half-wave plate immediately after the Kerr cell can be rotated to simulate the modification of polarization by the CO_2 light in the Kerr cell and to align the system. When its axis is in the same direction as the vertical polarizer, it has no effect on the transmission of the probe beam.

The second fiber optic also transmits green light from the doubled yag laser and provides a reference to account for modulation in the probe beam. Both fibers were imaged to points on the streak camera slit and streaked to a resolution of approximately 20 psec. The effect of temporal variations in the DCR11 pulse was removed by dividing the reference into the signal. Best results were obtained when we averaged the reference pulse over 150 psec and the signal over 20 psec to eliminate as much noise as possible while minimizing the effect on the 20 psec time resolution of the signal. The time resolution of our measurement is then the convolution of the streak camera resolution and averaging, i.e. 30 psec.

To determine the effect of the CO_2 laser or half-wave plate on the probe beam, we transform the probe beam coordinates $(\hat{x},\hat{y})$ into the bi-refringence coordinates $(\hat{x}',\hat{y}')$, include the phase change, and then convert back to the probe beam coordinates.

$$\hat{x} \Rightarrow \hat{x}' \cos(\theta) - \hat{y}' \sin(\theta) \qquad \hat{y} \Rightarrow \hat{x}' \sin(\theta) + \hat{y}' \cos(\theta) \qquad (A.2)$$
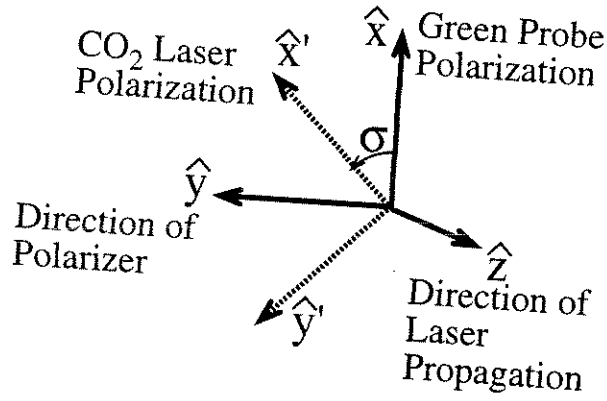
Figure A.4: Diagram of polarizations of CO_2 and green probe beam

$$\hat{x}' \Rightarrow \hat{x}\cos(\theta) + \hat{y}\sin(\theta) \qquad \hat{y}' \Rightarrow -\hat{x}\sin(\theta) + \hat{y}\cos(\theta) \qquad (A.3)$$

Phase shift:

$$\Delta n_{x'} = n_2 I, \; k = \frac{2\pi n}{\lambda_{gr}} \Rightarrow \Delta k_{x'} = \frac{2\pi}{\lambda_{gr}} n_2 I \qquad (A.4)$$

where $\Delta n_{x'}$ is the change in the index of refraction in the direction of polarization of the CO_2 laser, and $\Delta k_{x'}$ is the shift in phase of the probe beam per unit length caused by the this change in index of refraction.

$$\text{Let } h = \frac{\Delta k}{2}, \; \psi = kz - wt, \; \psi' = (k + \frac{\Delta k}{2})z - wt \qquad (A.5)$$

The electric field of the probe beam is:

$$E_{gr} = \frac{A}{2}\hat{x}e^{i\psi} + c.c. \Rightarrow \frac{A}{2}[\hat{x}'e^{ihz}\cos(\theta) - \hat{y}'e^{-ihz}\sin(\theta)]e^{i\psi'} + c.c. \qquad (A.6)$$

After propagating a distance L through the Kerr medium:

$$E_{gr}(z) = \frac{A}{2}e^{i\psi'}\left(\hat{x}[e^{ihL}\cos^2(\theta) + e^{-ihL}\sin^2(\theta)] + \hat{y}[e^{ihL} - e^{-ihL}]\sin(\theta)\cos(\theta)\right) + c.c$$

$$(A.7)$$

Ratio of transmitted light to incident light after $\hat{y}$ component is selected by the polarizer:

$$\frac{I_{tran}}{I_{inc}} = \frac{A^2}{2}4\sin^2(\theta)\cos^2(\theta)\sin^2(hL)/\frac{A^2}{2} = 4\sin^2(\theta)\cos^2(\theta)\sin^2(hL) \qquad (A.8)$$

Transmitted fraction of green probe light when co-propagating with the CO_2 beam of intensity I polarized 45° to the probe polarization:

$$\theta = 45°, \ h = \frac{n_2 I}{2} \frac{2\pi}{\lambda_{gr}} \Rightarrow T_{sig} = \frac{I_{tran}}{I_{inc}} = \sin^2(\frac{\pi}{\lambda_{gr}} n_2 I L) \qquad (A.9)$$

To calibrate the Kerr cell, we use a half-wave plate placed between the two
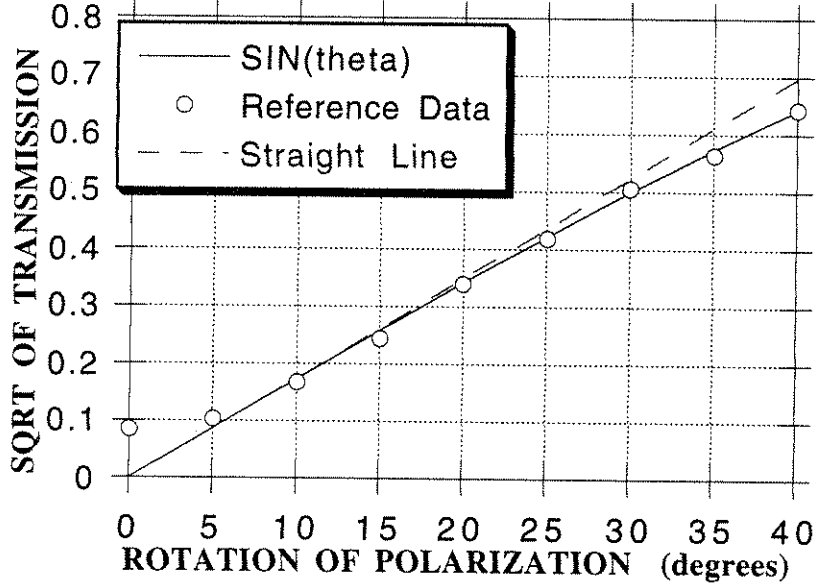

Figure A.5: Measurement of intensity versus rotation of polarization

polarizers rotated at an arbitrary angle θ. In this case:

$$hL = 90° \Rightarrow T_{ref} = \frac{I_{tran}}{I_{inc}} = 4\sin^2(\theta)\cos^2(\theta) = \sin^2(2\theta) \qquad (A.10)$$

For our experiment, $n_2 = 8.5 * 10^{-14}$ cm^2/W$= 2.2 * 10^{-20}$m^2/V^2, $\lambda_p = 532$ nm, $L = 5.4$ cm, and the transmission coefficient is $T_{sig} = \sin^2(\pi n_2 I L / \lambda_p) = \sin^2(2.7 * 10^{-8} I (W/cm^2))$. Using the relation $\sin(\theta) = \theta$ for small angles:

$$I = \sqrt{T}/2.7 * 10^{-8} \quad \text{for} \quad T < 1/4 \quad \text{(within 5\%)} \qquad (A.11)$$
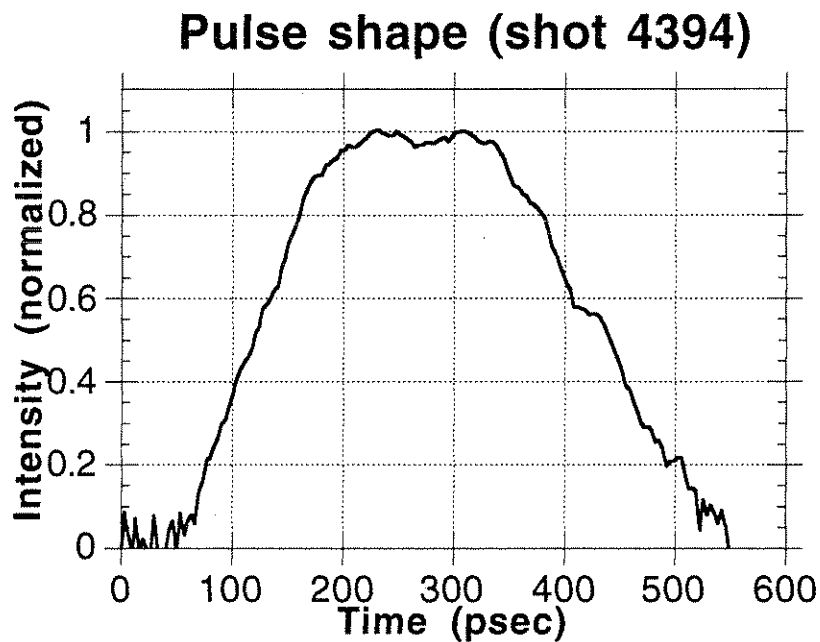
Pulse shape (shot 4394)

Figure A.6: Temporal Profile of Mars Laser Pulse

The half-wave plate placed directly after the Kerr cell allows us to calibrate the signal on the streak camera as a function of Kerr cell transmission. By rotating the half-wave plate and firing the DCR11 without the Mars Laser, the data in figure A.5 was obtained. The transmission through the second polarizer as a function of half-wave plate rotation has the same form ($T = sin^2(2\theta)$) as that for the Kerr cell. Therefore, as the graph is linear (within 5%) for small angles ($2\theta < 30°$), our data for the CO_2 intensity should be accurate over this region. Because the signal level is proportional to the square of the CO_2 laser intensity, the dynamic range of our measurement is limited to half that of the streak camera. This effect is clear in the half-wave plate data where a rotation in polarization of less than 5° is in the noise of the streak camera. This limitation does not effect our measurement of the FWHM of the pulse. The temporal profile

of a typical pulse is shown in figure A.6. At 350±70 psec, the laser pulses were about 75 psec longer than predicted by theory, but still short enough for doing the experiments of interest.

In the near future we plan to measure the pulses using sum frequency optical mixing of the CO_2 wavelengths with visible light from a laser diode, a much more sensitive diagnostic. This diagnostic will show any pedestals under the laser pulses and allow us to measure the laser pulses before the main amplifier, making a thorough study and optimization of the laser system much easier.

A.2   Transverse Profile of Focused Mars Laser

The profile of our laser beam at focus was determined experimentally by measuring the diameter of the beam above a threshold intensity on burn paper as the attenuation in the laser beam was varied. Assuming a symmetric spot, we obtained the experimental data points for the spot profile shown in figure A.7 where the intensity in arbitrary units is actually the attenuation in the laser beam. The horizontal error bars are the inaccuracy in measuring the diameter of the burns. The center point has vertical error bars rather than horizontal ones because it is not determined by the diameter of a burn. As there was no burn at an attenuation of 16, the intensity on axis must be between $8\sqrt{2}$ and 16. The central point is at the average of these two values with error bars stretching over the uncertainty.

When we fitted these points to a Gaussian, we found that the waist, w_0, was 150 μm. However, the pulse was actually much more flat-topped than a Gaussian, which is important as the intensity gradients determine the ponderomotive blowout of the plasma by the laser. To calculate a more realistic profile of the laser
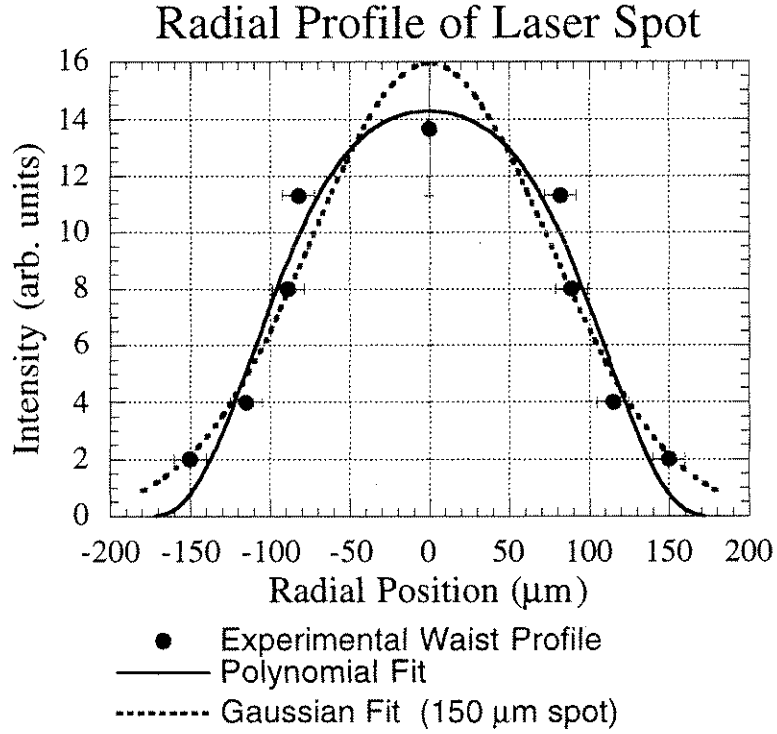
85

Radial Profile of Laser Spot

Figure A.7: Fitting of Laser Spot Profile

for use in simulations, we used a fourth order polynomial in r^2 with the boundary conditions that the peak intensity be normalized to 1 on axis that the amplitude and slope of the intensity be zero at a given distance $r = R$. The polynomial is chosen to be even as the beam should be symmetric around $r = 0$. Thus, our fitting polynomial is:

$$1 + a_1 \left(\frac{r}{R}\right)^2 + a_2 \left(\frac{r}{R}\right)^4 + a_3 \left(\frac{r}{R}\right)^6 + a_4 \left(\frac{r}{R}\right)^8 \tag{A.12}$$

Setting this and its derivative to zero at $r = R$:

$$1 + a_1 + a_2 + a_3 + a_4 = 0 \tag{A.13}$$

$$a_1 + 2a_2 + 3a_3 + 4a_4 = 0 \tag{A.14}$$

Solving these equations for a_1 and a_2:

$$a_1 = a_3 + 2a_4 - 2 \qquad (A.15)$$

$$a_2 = 1 - 2a_3 - 3a_4 \qquad (A.16)$$

These results can then be placed in kaleidagraph and solved for m_1 and m_2 as:

$$1 + (m_1 + 2m_2 - 2)\left(\frac{r}{R}\right)^2 + (1 - 2m_1 - 3m_2)\left(\frac{r}{R}\right)^4 + m_1\left(\frac{r}{R}\right)^6 + m_2\left(\frac{r}{R}\right)^8 \quad (A.17)$$

For the measured spot profile:

$$m_1 = 5.0168 \qquad m_2 = -1.9976 \qquad R = 176.88\mu\mathrm{m} = 3.22c/w_p \quad (A.18)$$

Putting this back into the original equation:

$$a_1 = -0.9784 \qquad a_2 = -3.0408 \qquad a_3 = 5.0168 \qquad a_4 = -1.9976 \qquad (A.19)$$

As shown in the figure, this curve fits the measured profile quite closely, much better than the Gaussian fit. It also has the advantage that the laser spot ends cleanly at $r = R$, eliminating problems with an abrupt cut off at the edge of the simulation.

A.3 Calculation of V_{osc} for Mars Laser

An important parameter for the beat-wave experiments is the intensity of the laser in v_{osc}/c unit. Following is a quick estimation of that intensity for a focused CO_2 laser pulse with 150 psec rise, 300 psec fall, 60 Joules, and $\mathrm{w}_0 = 150$ um spot size

Power = 60 J / 225 psec = $2.7 * 10^{11}$ Watts

$$I = I_p \exp\left[-2\left(\frac{r}{\mathrm{w}_0}\right)^2\right] \qquad (A.20)$$

$$P = I_p \int 2\pi r \exp\left[-2\left(\frac{r}{\mathrm{w}_0}^2\right)\right] dr = \frac{\pi \mathrm{w}_0^2}{2} I_p \qquad \text{(A.21)}$$

$$I_p = \frac{2 * 2.7 * 10^{11}}{\pi 0.015^2} = 7.54 * 10^{14} \text{ W/cm}^2 \qquad \text{(A.22)}$$

$$I = \frac{1}{2}\sqrt{\frac{\epsilon}{\mu}} E^2 \qquad \text{(A.23)}$$

$$E = \left(2 * 377 * 7.54 * 10^{14}\right)^{1/2} \text{ V/cm} = 7.54 * 10^8 \text{ V/cm} \qquad \text{(A.24)}$$

$$\frac{V_{osc}}{c} = \frac{eE}{mwc} = \frac{1.6 * 10^{-19} * 7.54 * 10^{10}}{9.11 * 10^{-31} * 1.78 * 10^{14} * 3 * 10^8} = 0.25 \qquad \text{(A.25)}$$

Appendix B

Beat-wave Issues

B.1 Ponderomotive Force

The ponderomotive force is very important for the beat-wave accelerator both as the driving force which creates the beat-wave and because it expels the plasma, causing the density to decrease over time. As the experiment is in cylindrical geometry (i.e. focused by a spherical lens) while the PIC code WAVE which is used to simulate the plasma beat-wave is in cartesian coordinates (equivalent to being focused by a cylindrical lens), it is important to determine the ponderomotive in both coordinate systems and see what the similarities and differences are. As the ponderomotive force is proportional to the gradient of the intensity of the laser, we first determine the laser profile in Cartesian and cylindrical coordinates. The full ponderomotive force of the laser is then calculated including the beat between the two laser frequencies. Finally, the decrease in plasma density due to blow-out of the electrons by the ponderomotive force before the ions begin to move is calculated, showing that the decrease in plasma density is negligible on time scales shorter than an ion period.

B.1.1 Profile of Electric Field

Beam Focused By Spherical Lens:

$$E = \left(\frac{w_o}{w(z)}\right) \exp\left(\frac{-r^2}{w^2(z)}\right) E_o \tag{B.1}$$

$$= \left[\left(\frac{w_o}{w(z)}\right)^{1/2} \exp\left(\frac{-x^2}{w^2(z)}\right)\right]\left[\left(\frac{w_o}{w(z)}\right)^{1/2} \exp\left(\frac{-y^2}{w^2(z)}\right)\right] E_o \tag{B.2}$$

$\Rightarrow$ Beam focused by cylindrical lens

$$E = \left[\left(\frac{w_o}{w(z)}\right)^{1/2} \exp\left(\frac{-y^2}{w^2(z)}\right)\right] E_o \tag{B.3}$$

B.2 Calculation of Ponderomotive Force

Let $a = eE/mw = a_1 \cos(w_1 t - k_1 z) + a_2 \cos(w_2 t - k_2 z)$. Here a is the v_{osc} of the laser.

$$\text{Ponderomotive Force:} \qquad F = -m\nabla(a^2/2) \tag{B.4}$$

$$a^2 = \frac{a_1^2 + a_2^2}{2} + 2a_1 a_2 \cos(w_1 t - k_1 z)\cos(w_2 t - k_2 z) \tag{B.5}$$

$$\cos(a)\cos(b) = \frac{\cos(a+b)}{2} + \frac{\cos(a-b)}{2} = \frac{\cos(a-b)}{2} \quad \text{(dropped high freq.)} \tag{B.6}$$

$$\Rightarrow a^2 = \frac{1}{2}(a_1^2 + a_2^2) + a_1 a_2 \cos(\Delta w t - \Delta k z) \tag{B.7}$$

Cylindrical Coordinates (Spherically focused laser)

$$F_z = -\frac{m}{2}\left(\frac{w_o}{w(z)}\right)^2 \exp\left(\frac{-2r^2}{w^2(z)}\right) a_1 a_2 \Delta k \sin(\Delta w t - \Delta k z) \tag{B.8}$$

$$F_r = \frac{m}{2}\left(\frac{w_0}{w(z)}\right)^2 \exp\left(\frac{-2r^2}{w^2(z)}\right) \hat{r}\frac{4r}{w^2(z)}\left[\frac{1}{2}(a_1^2 + a_2^2) + a_1 a_2 \cos(\Delta w t - \Delta k z)\right] \tag{B.9}$$

for $t_{rise} < t < t_{rise} + t_{fall}$. For the WAVE simulations the electron and ion thermal velocities $\sqrt{2KT/m}$ were $0.01c$ and $10^{-5}c$ respectively. This corresponds to an electron temperature of 26 eV with cold ions.

In Figs. B.4 (a) and (b), the sheet model is benchmarked against WAVE for a Gaussian profile $w_0 = 150$ μm spot size laser in Cartesian coordinates. This comparison shows that the sheet model matches the PIC simulations well, the only differences being slightly less noise in the sheet model and a narrower density spike at the edge of the laser profile in the sheet model. The density spike is broader in WAVE because of pressure effects which are ignored in the sheet model. The two simulations have the same density contours in the central region of the plasma, important for the beat-wave, because the density gradients are much smaller and the ponderomotive force dominates over the pressure terms.

To further evaluate the expulsion of the plasma, the sheet model is extended to cylindrical geometry with the same Gaussian laser profile in Fig. B.4 (c). evaluated in cylindrical geometry. Switching from Cartesian to cylindrical coordinates causes the plasma density to decrease much more rapidly because the plasma has two dimensions to expand into rather than only one. As the actual focused laser profile is not Gaussian, Fig. B.4(d) shows the effect of using the actual measured laser profile (Fig A.7) in cylindrical coordinates instead of the Gaussian profile from WAVE. The density in the central region where the beat-wave grows appears to decrease more slowly for the actual experimental parameters of Fig. B.4(d) than for the WAVE simulation parameters of Fig. B.4(a). This is consistent with the experimental results showing a longer beat-wave duration and slower density decrease than in the simulations.

The difference between Figs. B.4 (c) and (d) makes it clear that small changes

in the transverse profile of the laser at focus have a large effect on the rate of density decrease caused by ponderomotive blow-out. If the intensity profile were truly flat-topped with no gradients near the center, there would be no decrease in plasma density on axis until the plasma etched away from the edges.

Bibliography

[1] T. Tajima and J. M. Dawson. Laser electron accelerator. *Phys. Rev. Lett.*, 43(4):701–705, Jul 1979.

[2] C. E. Clayton et al. Relativistic plasma-wave excitation by collinear optical mixing. *Phys. Rev. Lett.*, 54(21):2343–6, May 1985.

[3] A. E. Dangor et al. Observation of relativistic plasma waves generated by the beat-wave with 1 μm lasers. *Physica Scripta*, T30:107–9, 1990.

[4] Y. Kitagawa et al. Beat-wave excitation of plasma waves and observation of accelerated electrons. *Phys. Rev. Lett.*, 68:48–51, Jan 1992.

[5] F. Amiranoff et al. Observation of modulational instability in Nd-laser beat-wave experiments. *Phys. Rev. Lett.*, 68:3710–3, June 1992.

[6] M. J. Everett et al. Dynamics of the resonantly excited relativistic plasma wave driven by a CO_2 laser. *Submitted to Phys. Plasmas*.

[7] R. L. Williams et al. Studies of relativistic wave-particle interactions in plasma-based collective accelerators. *Lasers and Particle Beams*, 8(3):427–49, 1990.

[8] M. J. Everett et al. Trapped electron acceleration by a laser-driven relativistic plasma wave. *Nature*, 368:527–529, Apr 1994.

[9] C. Darrow et al. Saturation of beat-excited plasma waves by electrostatic mode coupling. *Phys. Rev. Lett.*, 56(24):2629–32, Jun 1986.

[10] P. K. Kaw et al. Quasiresonant mode coupling of electron plasma waves. *Phys. Fluids*, 16(11):1967, 1973.

[11] M. J. Everett et al. Coupling between high-frequency plasma waves in laser-plasma interactions. *Submitted to Phys. Rev. Lett.*

[12] M. J. Everett et al. Evolution of stimulated Raman into stimulated Compton scattering of laser light via wave-breaking of plasma waves. *Submitted to Phys. Rev. Lett.*

[13] A. M. Sessler. New particle acceleration techniques. *Phys. Today*, 41(1):26–34, Jan 1988.

[14] C. Joshi et al. Ultrahigh gradient particle acceleration by intense laser-driven plasma density waves. *Nature*, 311:525–9, Oct 1984.

[15] M. N. Rosenbluth and C.S Liu. Excitation of plasma waves by two laser beams. *Phys. Rev. Lett.*, 29:701–705, Sep 1972.

[16] L. V. Keldysh. Ionization in the field of a strong electromagnetic wave. *Soviet Physics JETP*, 20(5):1307–14, May 1965.

[17] Frank Chen. *Introduction to plasma physics and controlled fusion.* Plenum Press, New York, New York, 1984.

[18] C. Joshi et al. Resonant self-focusing of laser light in a plasma. *Phys. Rev. Lett.*, 48(13):874–7, Mar 1982.

[19] E. A. Jackson. Nonlinear oscillations in a cold plasma. *Phys. Fluids*, 3(5):831, 1960.

[20] P. Sprangle et al. Nonlinear interaction of intense laser pulses in plasmas. *Phys. Rev. A*, 41(8):4463–9, Apr 1990.

[21] J. M. Dawson. Nonlinear electron oscillations in a cold plasma. *The Physical Review*, 113:383–387, Jan 1959.

[22] W. B. Mori. On beat wave excitation of relativistic plasma waves. *IEEE Trans. Plasma Sci.*, PS-15:88–106, 1987.

[23] R. J. Noble. Plasma-wave generation in the beat-wave accelerator. *Phys. Rev. A*, 32(1):460–71, Jul 1985.

[24] D. M. Villeneuve et al. Collective Thomson scattering in a laser-produced plasma resolved in time, space, frequency, or wave number. *J. Opt. Soc. Am. B*, 8(4):895–902, Apr 1991.

[25] C. E. Clayton et al. Novel small-angle collective Thomson scattering system. *Appl. Optics*, 24(17):2823–6, Jan 1985.

[26] R. E. Slusher and C. M. Surko. Study of density fluctuations in plasmas by small-angle CO_2 laser scattering. *Phys. Fluids*, 23(3):1974–1983, Mar 1980.

[27] R. L. Morse and C. W. Nielson. Numerical simulation of the Weibel instability in one and two dimensions. *Phys. Fluids*, 14(4):830, Apr 1971.

[48] W. P. Leemans et al. Plasma physics aspects of tunnel-ionized gases. *Phys. Rev. Lett.*, 68(3):321–4, Jan 1992.

[49] T. P. Coffey. Breaking of large amplitude plasma oscillations. *Phys. Fluids*, 14(7):1402–6, Jul 1971.

[50] S. Qian and D. Chen. Discrete Gabor transform. *IEEE trans. on Signal Proc.*, 41(7):2429–39, Jul 1993.

[51] Joseph T. Verdeyen. *Laser Electronics*. Prentice-Hall, Inc., Englewood Cliffs, New Jersey, 1981.

[52] M. A. Duguay and J. W. Hansen. Ultrahigh-speed photography of picosecond light pulses. *IEEE J. Quantum Electron.*, QE-7(1):37, Jan 1971.